◨ NTNU

Norwegian University of
Science and Technology

Oxide Hydrogen Interaction and Porosity Development in Al-Si Foundry Alloys

Behzad Mirzaei

Light Metals Production
Submission date: September 2011
Supervisor: Ragnhild Aune, IMTE

Norwegian University of Science and Technology
Department of Materials Science and Engineering

To my Parents,

Without whom I wouldn't be

Statutory Declaration

I declare that I have developed and written the enclosed thesis entirely by myself and have not used sources or means without declaration in the text. Any thoughts or quotations, which were inferred from these sources, are clearly marked as such.

This report was not submitted in the same or in a substantially similar version, not even partially, to any other authority to achieve an academic grading and was not published elsewhere.

Trondheim- Sep 2011

Behzad Mirzaei

Acknowledgements

My appreciation and gratitude are conveyed to the people listed below, who all contributed to the work presented in this thesis.

Professor Ragnhild E. Aune, my supervisor, for giving me the opportunity to work with things I care a great deal about, your knowledge and passionate guidance throughout the work. I am truly grateful.

Many thanks go in particular to co-supervisor Dr. Shahid Akhtar, for his great support, guidance. I am much indebted to Shahid for his valuable advice in science discussion, supervision in experiments and furthermore, using his precious times to read this thesis and gave his critical comments about it.

All unmentioned colleagues at the Division of Materials Science and Engineering for offering such a friendly and supportive working atmosphere.

Abstract

Aluminium alloys based on the aluminium-silicon system are increasingly being used in the automotive and aerospace industry due to high strength to weight ratio.

Absorption of hydrogen in the aluminium melt, formation of oxide films, and their interaction are generally accepted as one the main reasons for formation of porosities. Oxide layers entrapped by the surface turbulence; folded in the melt and eventually becomes a submerged film and behaves like a crack. This mechanism caused a surface folded over against itself with gas trapped in between two halves, called *bifilm*. During solidification, hydrogen will be segregated and diffused into bifilms and caused expansion of bifilm and form porosity. These porosity type defect acts like a stress riser and had detrimental effect on static and dynamic mechanical properties. This research investigates the influence that different levels of entrained oxides have on the properties essential for obtaining high quality aluminium castings under constant hydrogen concentration.

Two levels of oxide were introduced into the A356 melt by the addition of anodized plates and oxide rods. Set of reference castings have been also produced without any addition of oxides in A356 alloy. Different series of casting have been produced from each melt which include bars for tensile testing, bend sample plates. The castings were characterized in terms of microporosity and mechanical properties. Reduced pressure test (RPT), Porous disc filtration apparatus (PoDFA) test were performed to investigate the melt quality. The main factor which altered the formation and distribution of porosity is double oxide layers, since the effect of hydrogen was constant. The results showed the tensile and bend properties of casting samples were affected by additional oxides.

Table of Contents

List of Illustrates

List of Tables

1 Introduction

Formation of defects, such as segregation, inclusions, and porosity, during the solidification of aluminium alloys can dramatically affect the engineering properties of the finished products. Increasing demand for use of aluminium foundry alloys in the production of critically stressed components in the automotive and aerospace industries, marine engines, building structures, as well as for the small components for appliances and hand tools has led aluminium industry to focus sharply on quality and reliability of such component castings.

The casting processes itself may introduce many defects, such as bubble trails, segregation, gas porosity, shrinkage cavity, residual stress, hot tear and cold crack. These defects like bi-films mainly form at the melting stage and handling of the melts in the casting process. The defects like oxide films are either present in the original alloy or created during the casting process, which may be incorporated in the final microstructure and decrease the component's properties and life time. Therefore, it is essential that the quality of the product begins with the quality control of the melt.

One of the biggest issues in aluminium castings is oxide films. During the production of aluminium castings, the surface oxide on the liquid may be folded in to the bulk liquid and it causes many crack-like defects that are extremely thin, also known as '*bifilm*' are held responsible for the potential failure mechanisms. Bifilms and dissolved hydrogen play the major role in forming porosity during solidification.

The present study examines the influence of different levels of entrained oxides to obtain high quality aluminium castings under constant hydrogen concentration.

The oxide level of an A356 aluminium alloy were increased by (i) additions of anodized aluminium plates for increasing the bi-films levels in the melt, and by (ii) additions of an extruded aluminium oxide rod directly to the melt. A clean A356 melt (no additions of any particulates) were used as reference material. The melting experiments were conducted in an electric resistance furnace under carefully controlled conditions.

From each of the melts a series of reproducible castings were made for tensile test and bend tests. For the evaluation of melt quality, in terms of inclusion count and bi-films index, the Porous Disc Filtration Apparatus (PoDFA) and the Reduced Pressure Test (RPT) were adopted. For the analysis of fracture behavior Scanning Electron Microscopy (SEM) was used. The dissolved hydrogen level were measured by adopting an ALSPEK* H probe.

A brief introduction as a background and a framework for the other chapters is given in the chapter two. It is an introductory presentation of melt quality, impurities, defects, mechanical properties, and the important parameters related to bifilms and porosities.

In chapter 3, the experimental techniques such as ALSPEK* H Probe, PoDFA, RPT, Image Analysis, and mechanical tests used in current study are presented.

The interpretations of results and discussion on the results are addressed in Chapter 4.

Finally, chapter 5 presents the main conclusion.

1.1 Industrial Motivation

There is growing evidence of reports that aluminium castings under-perform by a large margin [1]. This is mainly due to presence of detrimental defects, particularly bifilms, which are held responsible for formation of porosity and low mechanical properties. The bifilms may or may not expand enough to form porosity, but they present the ultimate challenge in today's aluminium castings process and are held responsible for many products failures, such as low mechanical properties, low fatigue properties and reduced elongation. Furthermore, due to the growing trend in the aluminium applications, industry is forced to make considerable effort to control and minimize these defects that are formed in the aluminium and its alloys during the casting process and responsible for reduction in melt quality. Accordingly, the aluminium industry needs to focus on the quality parameters such as hydrogen content, and bifilms [2-3].

2 Literature Review

With increase in public concerns for environmental and energy issues have led manufacturing industry to a debate about energy resources and the efficient use of energy. Aluminium is found to be a perfect material in so many industries due to its exceptional properties and it plays a major role in adapting the equipments to tomorrow's needs [4-5].

Exceptional properties of aluminium alloys, such as its lightweight, strength, recyclability, corrosion resistance, durability, ductility, formability and conductivity, make it one of the most valuable materials among the economically important metals such as iron, manganese, and zinc. Due to great versatility and unique combination of properties, the variety of applications of aluminium continues to increase. Aluminium offers countless possibilities and applications in our daily live; planes, trains, cars, ferries, heat and light appliances, electronic and computer components, food processing equipment, beverage cans, and foil of thickness down to 5 µm are using from different kinds of aluminium [5].

Aluminium alloys can be cast by almost all casting processes, such as sand casting, permanent mould, and high pressure die casting; which are highly productive and cost efficient processes. In the recent years there has been an increase in the use of low pressure die casting and thixocasting processes. The major alloy systems used for shaped castings are aluminium-copper, aluminium-magnesium and aluminium-silicon alloys. Eutectic and hypoeutectic aluminium alloys are by far the most important commercial alloys due to their superior casting properties, like good fluidity, coupled with good mechanical properties [6].

2.1 Metal Quality

Most of liquid metals contain different kind of oxide, carbide, and boride impurities, and defect formation during casting is an inevitable consequence of the presence of these impurities [7]. It is important to know the main source of these impurities, as mentioned in

table 2-1. Some impurities come from extracting pure metal from ores and raw materials, in the extractive metallurgy processes. Impurities and inclusions may also introduce from refractories, atmosphere during the production of the metal, slag particles, and even in the refining processes. The aluminium from the Héroult-Hall electrolysis cell contains usually about 0.01% Na, 0.01% V, and 0.5 p.p.m H, in addition to 0.1% Fe and 0.04% Si [8]. Moreover, a typical aluminium melt contains a large number of small non-metallic inclusions, less than or equal to 50 μm in size. These include particles of oxides (Al_2O_3), spinels ($MgAl_2O_4$), and carbides (SiC, Al_4C_3), with a higher melting point than the host metal. These inclusions in alloys reduce mechanical properties, are detrimental to surface finish and increase porosity, as well as having a tendency to increase corrosion. Non-metallic inclusions act as stress raisers, and can cause premature failure of a component [9].

In addition to solid impurities oxygen, hydrogen, and nitrogen may enter the molten metal and affect the mechanical properties of the cast metal. Aluminium has a high affinity to oxygen, therefore oxide particles and films are often the most common inclusions observed within aluminium melts [8]. The driving force for these processes is the striving of the melt to come into equilibrium with its surroundings [7].

Accordingly, there are three important features that define metal quality: trace elements, dissolved gas, and non-metallic inclusions [10]. During solidification as the temperature drops and solubility decreases inclusions are partly participated, as a non-metallic or intermetallic phases, in the metal [8]. Table 2-1 lists some of the common inclusion sources in aluminium alloys.

The detrimental effect of defects not only depends on their distribution and morphology in the microstructure and these features may also vary with casting and solidification parameters. Moreover, the presence of these defects makes materials properties unpredictable [11].

Table 2-1 Source of inclusions in aluminium [7-8]

Inclusion Type	Possible Origin	Typical Size (Microns)	Typical Concentration (p.p.m)
Carbides (Al_4C_3)	Pot cells from Al smelters	1-20	5
Borides (TiB_2)	From grain refiner	1-3	10-50
Borides (VB)	From Hall-Heroult cell	1	0.5
Boro-Carbides (Al_4B_4C)	Boron treatment		
Graphite (C)	Fluxing tubes, Rotor wear, Entrained film		
Chlorides (NaCl, KCl)	Chlorine or fluxing treatment		
Magnesium Oxide (MgO)	Higher Mg containing alloys	1-100	0.01-2
Alpha Alumina (α-Al_2O_3)	Entrainment after high-temperature melting	10-20	0.01
Gamma Alumina (Y-Al_2O_3)	Entrainment during pouring		
Spinel ($MgOAl_2O_3$)	Medium Mg containing Alloys		
Refractories		100-500	0.01

2.1.1 The Dissolution of Hydrogen

A liquid metal at high temperature is chemically reactive, so they are prone to considerable adsorption of gases, such as hydrogen, oxygen, and nitrogen. The gases absorbed by the surface of the metal are capable of diffusing into the metal in the atomic state [10,12]. The hydrogen content probably dominates in the casting aluminium and its main source is dissociation of water vapor. Sources of hydrogen contamination also include [13]:

- Atmosphere
- Incompletely dried refractories
- Remelt ingot, master alloys, metallurgical metals, and other charge components
- Fluxes
- Tools, flux tubes, and ladles
- Products of combustion (POCs) in gas-fired furnaces

This moisture can react with the molten aluminium:

$$H_2O\ (g) + \frac{2}{3}Al\ (l) \rightarrow \frac{1}{3}Al_2O_3 + 2H\ (in\ Al) \qquad\qquad \text{2-1}$$
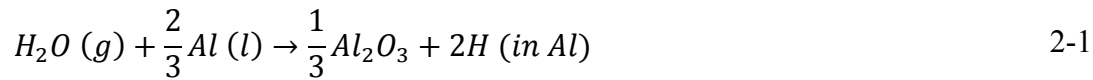
In the beginning, a small amount of metal reacts with penetrated gas to form oxide. As the result, hydrogen is released to equilibrate itself between the gas and metal phases [8]. Whether it will enter the metal or the gas above the metal will depend on the temperature and relative partial pressure of hydrogen already present in both of these phases. The molecular hydrogen has to split into atomic hydrogen before it can be taken into melt according to equation 2-2 [7]:

$$\frac{1}{2}H_2(gas) = H(in\ Al) \qquad\qquad \text{2-2}$$

The equation 2-3 shows the relation between partial pressure and concentration of hydrogen in equilibrium in the melt is:

$$[H]^2 = kP_{H_2} \qquad\qquad \text{2-3}$$

It is found that k is affected by alloying additions and temperature. Then, at constant partial pressure of hydrogen in a certain aluminium alloy, k is numerically depends on temperature. Figure 2-1 shows how the solubility of hydrogen in aluminium decreases with temperature. During solidification the liquid tries to keep itself in equilibrium with the environment above the liquid. Therefore, the liquid gradually lose its hydrogen atoms and this phenomenon continues until the rate of loss of hydrogen from the melt surface becomes equal to the rate of gain hydrogen that returns into the melt. Accordingly, the liquid always retains a certain amount of hydrogen, especially at higher partial pressure of hydrogen with respect to the liquid [7].

Because of small volume of atomic hydrogen, it can rapidly diffuse in liquid metal. The investigations [10] showed that diffusion through an alumina film is accomplished in the following stages:

"1. Dissociation of the molecular hydrogen;

2. Development of activated adsorption on the oxide surface;

3. Release of hydrogen from the adsorbed layer and its passage into true solution;

4. Movement of the dissolved hydrogen through the crystal lattice;

5. Passage of hydrogen into the absorbed layer on the opposite side of the film;

6. Desorption of atoms of hydrogen;

7. Transport by advection of the bulk liquid."
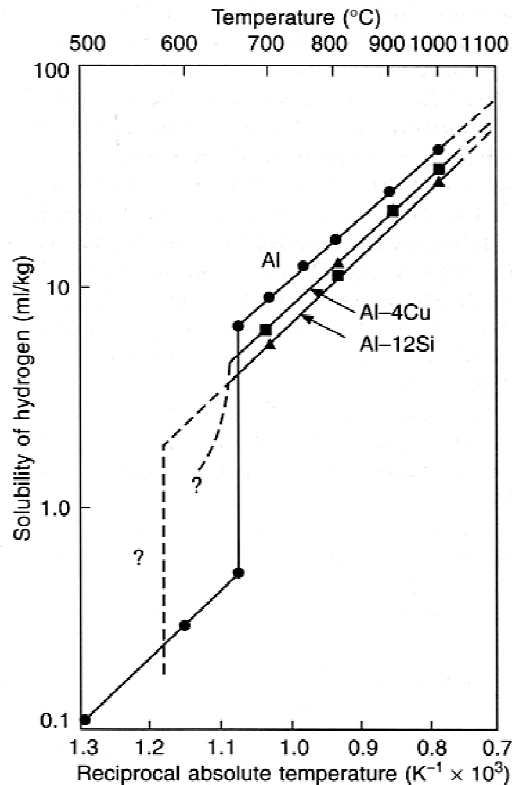
Figure 2-1 Hydrogen solubility in aluminium and two of its alloys [7]

Figure 2-2 illustrates the correlation between temperature and the hydrogen concentration, in the liquid and environment. The concentration of hydrogen in liquid aluminium increases with raising the temperature and with higher atmospheric moisture concentration. Therefore, during solidification, hydrogen may exceed the solubility limit and will be segregated ahead of the solidification front [14].

Degassing by the use of inert or active gases reduces hydrogen concentrations by diffusion into bubbles of the fluxing gas corresponding to the partial pressure of hydrogen in the fluxing gas. Spinning-rotor techniques have been developed that provide more intimate

mixing, efficient gas-metal reactions, and shorter reaction times to achieve low hydrogen levels. The use of active fluxing gases and filtration removes oxides, permitting acceptable quality castings to be produced from metal with higher hydrogen contents [13].
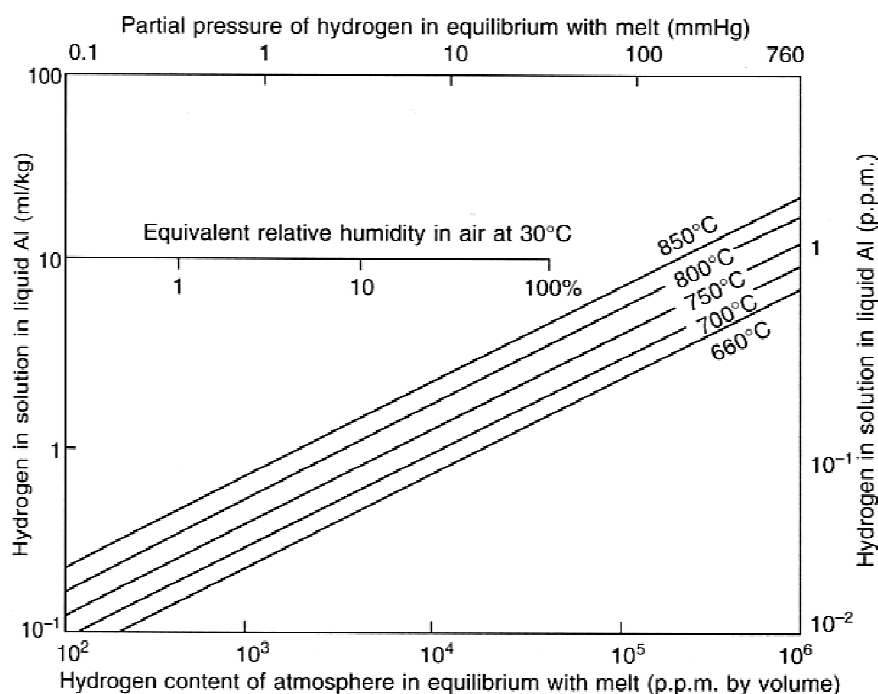
Figure 2-2 Hydrogen content of liquid aluminium shown as increasing with temperature and the hydrogen content of the atmosphere [7]

2.1.2 Formation of Oxide Film

The surface of liquid aluminium comprises an oxide film, although, the solubility of oxygen in aluminium is extremely low and the oxides certainly cannot have been precipitated by reaction with oxygen in solution. The surface turbulence folds the oxide layer in the bulk and a new oxide layer forms on the surface. Therefore, the motion of surface, as result of charging, fluxing, degassing, skimming, transferring, and mould filling, may leads to further oxidation and more entrained oxide in the bulk [7,14].

Based on an investigation of the process of oxidation of metals, it is established that the protective action of the film may be determined by the ratio of the molecular volume of the oxide to the atomic volume of the metal contained in the compound. If this ratio is greater

than unity, a dense continuous film is formed; if this ratio is less than unity, a discontinuous film is formed [10]:

$$\frac{w_o d_M}{W_M d_o} > 1 \qquad \textit{Continuous Film} \qquad 2\text{-}4$$

$$\frac{w_o d_M}{W_M d_o} < 1 \qquad \textit{Discontinuous Film} \qquad 2\text{-}5$$

$w_{o/M}$: *The molecular weight of the oxide/metal*

$d_{o/M}$: *Density of the oxide/metal*

During oxidation processes, a phase transformation occurred between different forms of aluminium oxide. The initial oxide film is an amorphous form of aluminium, but after a while transforms into crystalline alumina, named also gamma-alumina. These two different forms of aluminium oxide, probably only a few nanometers thick, keep the surface from further oxidation. However, after an incubation period the gamma alumina in turn transforms to alpha-alumina, which allows oxidation at a faster rate [7]. Figure 2-3 shows the rate of thickening of films on aluminium in relation with different environments.
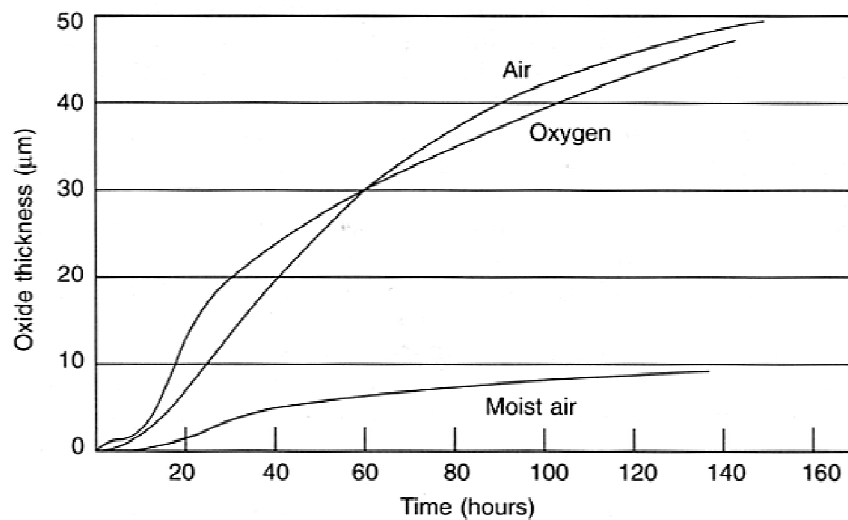
Figure 2-3 Growth of oxide on Al at 800° C in relation with different environment [7]

The majority of aluminium alloys have some magnesium in the range, 0.01-2 p.p.m. and it changes the melt behavior as its percentage increases. For instance, where the aluminium alloy contains less than approximately 0.005 weight percent magnesium the surface oxide is pure alumina. Above this limit the alumina can convert to the mixed oxide, $Al_2O_3.MgO$, known as spinel. First an alumina film forms almost immediately on a newly created surface, and with time it will always be expected to convert to a spinel film. Figure 2-4 shows the rate of growth of oxide on aluminium and its alloys.

According to preceding explanation, on the bright side, since the oxide itself is almost certainly fairly impervious to the diffusion of both metal and oxygen, it can protect the melt from further oxidation. On the dark side, the film is permeated with liquid metal, especially when it has been changed to porous spinel [7].
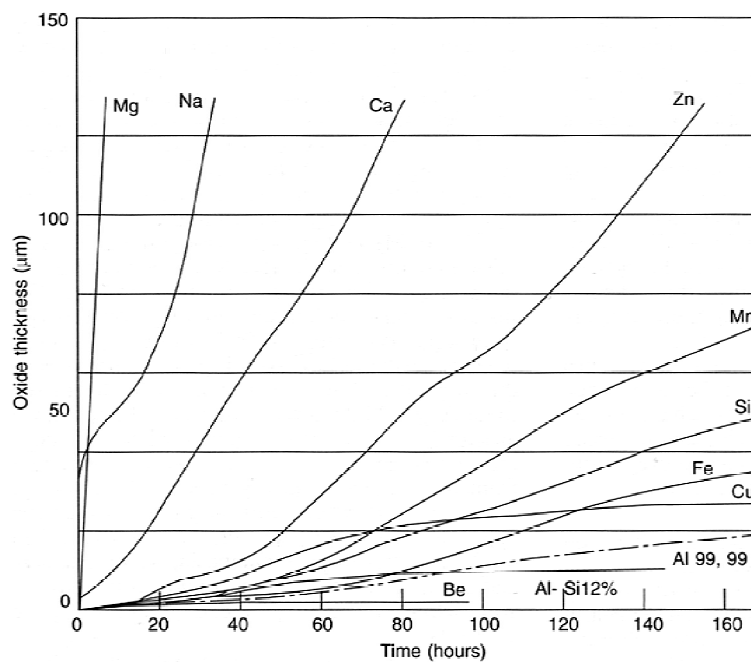
Figure 2-4 Growth of oxide on Al containing alloying elements [7]

2.2 Porosity Phenomena in Aluminium Alloys

In contrast to all defects in cast aluminium products, the porosity has been held responsible for the majority of failures [14-16]. Porosities have a negative effect, not only on the

mechanical properties but on the machinability and the surface properties of aluminium castings.

2.2.1 Porosity Classification in Aluminium alloys

Porosity formation in cast aluminium products can be categorized as follows:

1. **According to size:**

   - Microporosity (<100 µm)

   - Macroporosity (>100 µm)

Microposority is very small and almost invisible to naked eyes and it occurs in long freezing range alloys. Microporosities are well dispersed cavities and sometimes spherical in forms. Macroporosity occurs mainly in short freezing range alloys or pure metals and is characterized by the large cavities or pipes that form because of the shrinkage of the solidifying metal [6]. Figure 2-5 shows differences between microporosity and macroporosity.
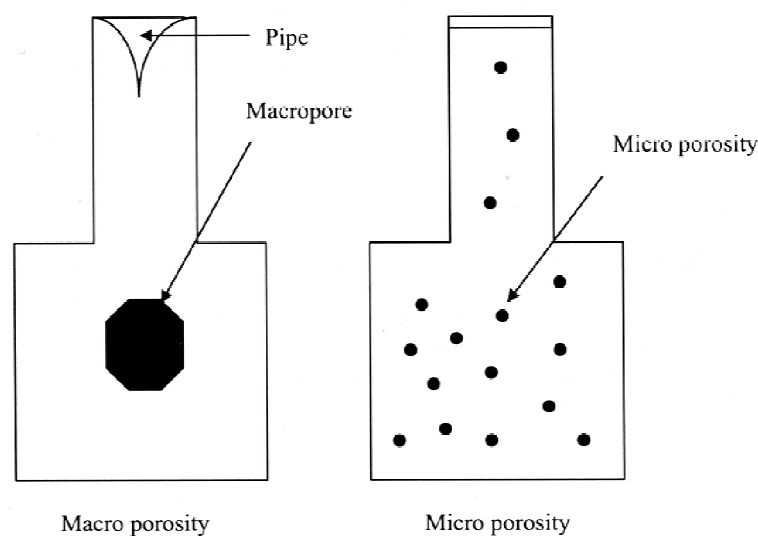
Figure 2-5 Difference between macro- and microporosity [6]

2. **According to cause:**

- Gas porosity

- Shrinkage porosity

The gas porosity, in contrast to shrinkage porosity, is generally round, isolated and well-distributed. It is formed during solidification, because of rejection of hydrogen from the melt. On the other hand shrinkage porosity is interconnected or clustered and of an irregular shape, corresponding to the shape of the interdendritic regions and mainly caused by the inability of the liquid metal to compensate the solidification contraction [6]. It is worth mentioning, according to figure 2-11, hydrogen porosity may grows along the dendritic arm regions and form a porosity look like shrinkage pores. This phenomenon added further complication to differentiating between the gas and shrinkage porosities.

2.2.2 Gas Porosity

Liquid aluminum reacts with water vapor found in the atmosphere to produce aluminum oxide and hydrogen gas according to the reaction 2-1. Hydrogen is the only gas that is appreciably soluble in aluminium and its alloys.

The solubility of hydrogen in aluminium varies directly with temperature and the square root of pressure. Hydrogen solubility is considerably greater in the liquid than in the solid state, figure 2-1. No more hydrogen than indicated in equilibrium condition can be dissolved at any temperature.

During solidification, with decreasing the solubility limit of hydrogen, the excess hydrogen rejected from the solidification front. At sufficiently high concentration of rejected hydrogen forms interdendritic porosity and resulting in critical porosity content. When the concentration of dissolved hydrogen is low, microporosity formation occurs at subcritical condition. Figure 2-6 shows the correlation between hydrogen amount and porosity fraction in different cooling rates.

Hydrogen bubble formation is strongly resisted tension forces, by increased liquid cooling and solidification rates that affect diffusion, and by an absence of nucleation sites for hydrogen precipitation such as entrained oxides. The precipitation of hydrogen obeys the laws of nucleation and growth and is similar in these respects to the formation of other metallurgical phases during solidification.

Kaufman and Rooy [13] have categorized the process of hydrogen precipitation to four stages and mentioned certain rules describe the tendency for hydrogen pore formation. These rules introduce a critical or threshold hydrogen value corresponds to pore size and volume fraction.

Just as in the case of crystal formation, hydrogen precipitation may occur as a result of heterogeneous or homogeneous nucleation. The most powerful nucleants for hydrogen precipitation are oxides, bifilms. In presence of such nuclei, hydrogen precipitates readily at even relatively low dissolved hydrogen levels. In the absence of nucleating phases such as oxides and gaseous species, surface tension forces are generally strong enough that precipitation is suppressed at even relatively high dissolved hydrogen levels.
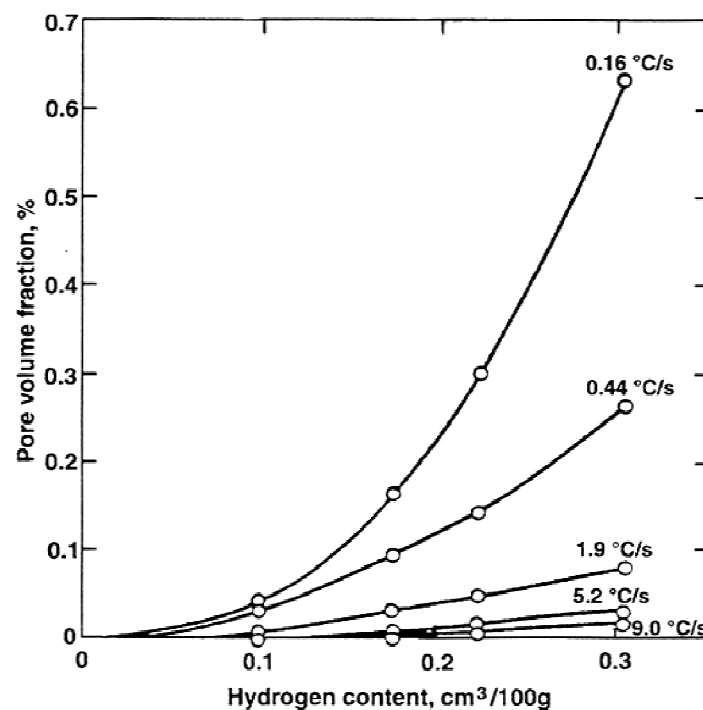
Figure 2-6 Hydrogen content, pore size, and cooling rate relationships in an Al alloy [13]

13

2.2.3 Shrinkage Porosity

For most metals, the transformation from the liquid to the solid state is accompanied by a decrease in volume. On the other side, the density in the solid is usually higher than in the liquid and it leads to molten metal flow towards the solidification front [17]. Therefore, shrinkage occurs during solidification can define as the result of volumetric or density differences between liquid and solid states. Two important parameters affect on forming the shrinkage porosity, first, the liquid/solid volume fraction at the time of final solidification, and the solidification temperature range of the alloy.

Most aluminium alloys have a long freezing range and flow through mushy zone becomes difficult [18]. Moreover, if the castings are not sufficiently fed in one or more regions, then internal hydrostatic tension increases, reaching a level at which an internal pore may form. In aluminium alloys, the volumetric shrinkage that occurs during solidification ranges from 3.5 to 8.5% [7].

Chambell classified shrinkage displacement into five modes [7] and figure 2-7 schematically illustrates each mode. Mass feeding and interdendritic feeding, are two important modes which take place in castings [13]:

- **Liquid feeding:** Bulk motion of the molten metal.

- **Mass feeding:** Mass feeding is liquid displacement occurring in the absence of substantial resistance. In these cases, pressure at the solidification interface and pressure in the riser system are essentially equivalent. Pressure drop develops as obstructions to the feeding path form.

- **Interdendritic feeding:** The progressive development of a dendritic network and localized solidification results in increased resistance to fluid flow until the pressure at the solidification front is reduced to zero, at which time a shrinkage void will form. Interdendritic feeding takes place in the interval between mass feeding and the point at which sufficient resistance develops that liquid flow through the solidifying dendrite network no longer occurs.

- **Burst feeding:** Hydrostatic tension may increases in poorly fed region of the casting and these results in collapse of the dendritic network to supply liquid metal.

- **Solid feeding:** This occurs when the incipient shrinkage void is filled by the collapse of surrounding solidified metal.
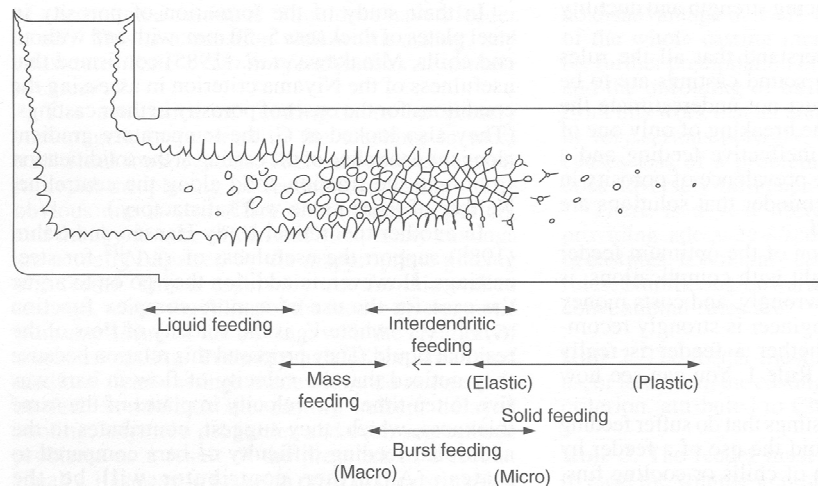
Figure 2-7 Schematic representation of the five feeding mechanisms in a solidifying casting [7]

In short solidification range alloys, such as A356 and 413, Directional solidification is highly probable. Defects may take the form of extensive piping as opposed to distributed shrinkage porosity, as shown in figure 2-8. These alloys may be characterized by a higher proportion of mass feeding relative to interdendritic feeding [13].
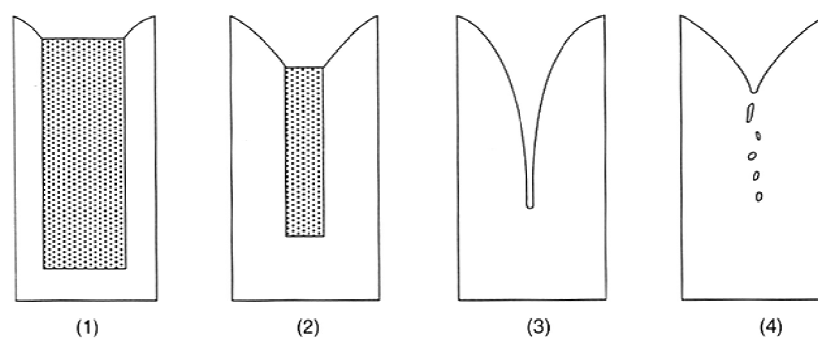
Figure 2-8 Stages in the development of a primary shrinkage pipe [7]

In long freezing range alloys, such as some aluminium-copper and aluminium-magnesium alloys, interdendritic shrinkage is more favorable. Microporosity extensively happens in these

alloys and it is because higher proportion of feeding that takes place interdendritically. Dendritic mush makes feeding more difficult and feeding through near isolated pools of liquid is more favorable than drawing liquid from a distinct feeder [6,13]. The effect is easily seen in figure 2-9, where in short freezing range alloy cavities prove that interdendritic liquid is being drained away from the surface. Figure 2-10 illustrates how the section thickness affects on origin of porosity. In the thin section, porosity content is negligible while in intermediate sections surface-linked porosity is more pronounced. Thick sections contain internally nucleated porosity [7].
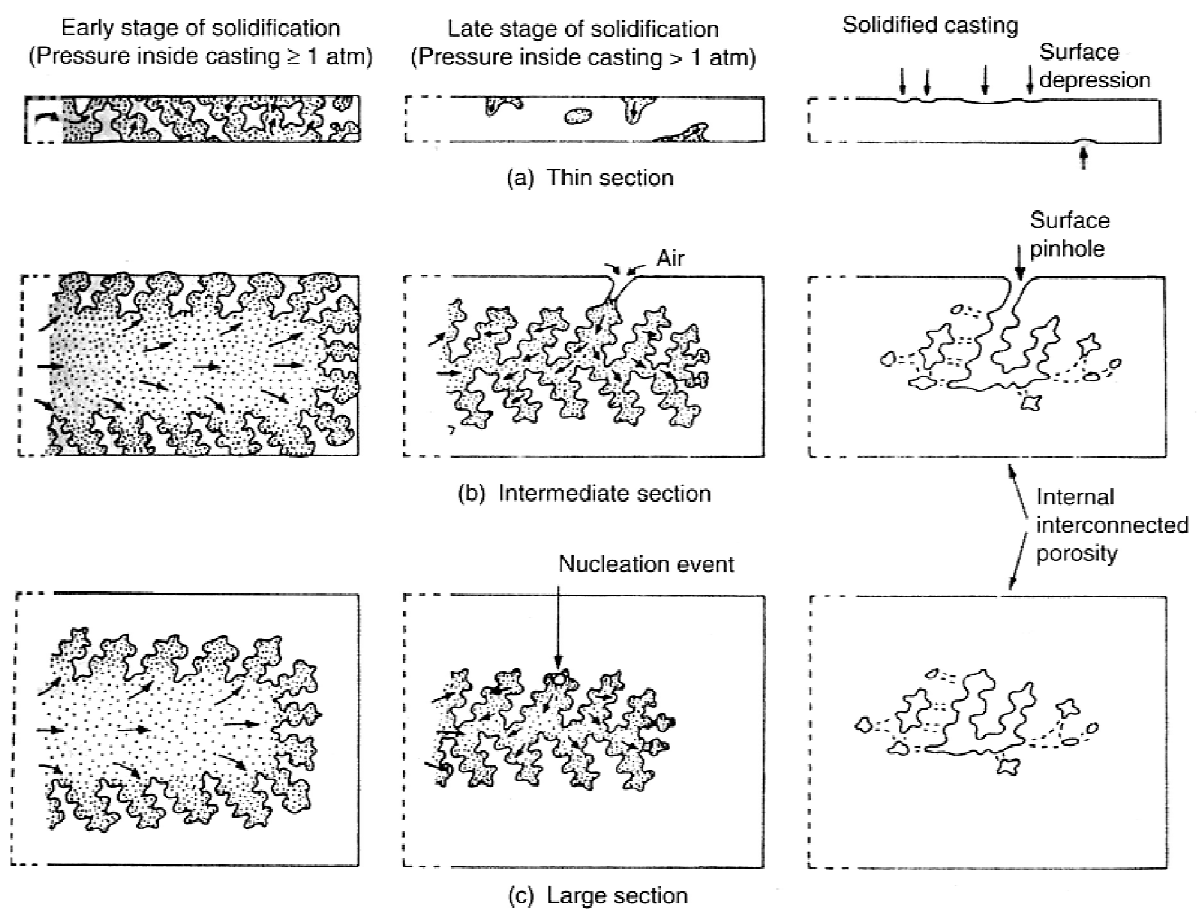
Figure 2-9 Schematic representation of the origin of porosity as section thickness is increased

The severity of shrinkage is increased by many factors including:

- Geometrical complexity
- Varying section thickness
- Solidification rate

- Alloy feeding characteristics
- Limitation in effective gating and risering practice that fail to provide the gradients required for directional solidification [6,13].

Shrinkage void fraction varies in proportion to the fourth root of the pressure, thus increasing pressure has little effect on shrinkage unless high pressures can be employed. Improved modification and refinement of aluminium-silicon alloys, improved grain refinement, and reduced oxide content all improved feedability and therefore reduce shrinkage severity [13].
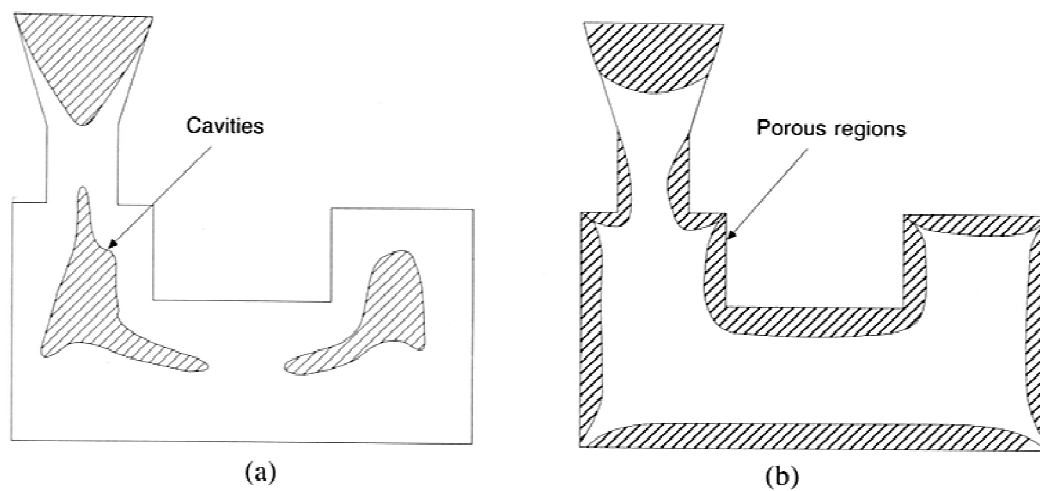
Figure 2-10 (a) internally pores in a short-freezing-range alloy; (b) externally in a long-freezing-alloy

2.2.4 Combined Effect of Hydrogen, Shrinkage, and Inclusions

Gas and shrinkage porosity formation are considered to be independent phenomena but there are interactive mechanisms that affect both [13].

The hydrogen solubility is reduced in the surrounding liquid, during solidification, facilitating the precipitation of hydrogen into the forming void. Therefore, dissolved hydrogen significantly increases shrinkage pore size. Then hydrogen has an addition effect on shrinkage porosity and cause a higher pore volume fraction.

On the other side, the formation of hydrogen voids and the effects of hydrogen on internal shrinkage are influenced by entrained inclusions. Because inclusions strongly facilitate bubble formation even at very low levels of dissolved hydrogen.

Porosity in castings, whether hydrogen voids, shrinkage, or defects that can be associated with both conditions, such as inclusions, can be understood and prevented by:

- Melt treatment must be performed for effective removal of oxides and other entrained nonmetallic and the reduction in dissolved hydrogen concentration.

- Metal handling, pouring, and the design of the gating system must preserve required molten quality.

- The gating and risering system with variable heat extraction techniques and application of the principles of directional solidification must be capable of minimizing or preventing shrinkage porosity [13].

2.3 Classical Theories of Porosity Formation

2.3.1 Homogeneous Nucleation

When a solid form within its own melt without the aid of foreign materials, it is said to nucleate homogeneously. Nucleation in this manner requires a large driving force due to the relatively large contributions of the surface energy to the total gibbs energy of very small particles. Precipitation of solid particles may take place to undercooling of the melt, or precipitation may be caused by addition or presence of impurities that react to a second phase [8].

Campbell, using the theory developed by fisher, gives following discussion of homogeneous nucleation. This theory tried to quantify the conditions required for the formation of porosity in liquid metals. A quantity of work is associated with the reversible formation of a bubble in a liquid. If the local pressure in the liquid is P_e, we need to carry out an amount of work $P_e V$ to push back the liquid far enough to create a bubble of volume V.

The formation and stretching out of the new liquid/gas interface of area A requires work γA, where γ is the interfacial energy per unit area. The work required filling the bubble with vapour or gas at pressure P_i is negative and equal to $-P_iV$. Thus the total work is [7]:

$$\Delta G = \gamma A + P_e - P_i \qquad \text{2-6}$$

$$= 4\gamma \pi r^2 + \frac{4}{3}\pi r^3 (P_e - P_i) \qquad \text{2-7}$$

Where clearly $(P_e - P_i)$ is the pressure difference between the exterior and the interior of the bubble. A plot of ΔG versus bubble radius r shows a maximum that constitutes an energy barrier to nucleation, figure 2-11 The maximum free energy ΔG^* and critical radius r^* in this case are:

$$\Delta G^* = \frac{16\pi \sigma^3}{3(\Delta p)^2} \qquad \text{2-8}$$

$$r^* = \frac{2\gamma}{\Delta p^*} \qquad \text{2-9}$$

It is worth mentioning that $r > r^*$ the negative slope increases with r. Then $-\Delta G^*$ attains a higher value for every molecule added. Thus a nucleus with radius r^* or greater can grow, while a particle smaller than r^* (cluster) tends to shrink since ΔG^* decreases with decreasing r. To find r^* the maximum for ΔG^* is determined [8]:

$$\frac{\partial \Delta G_n}{\partial r} = 0 \qquad \text{2-10}$$

Estimation of the number of critical nuclei in an aluminium melt indicates that formation of homogeneous nucleus is achievable only at saturation pressures of 5000-10000 bar. It follows from these considerations that homogeneous bubble formation is completely unrealistic [19].
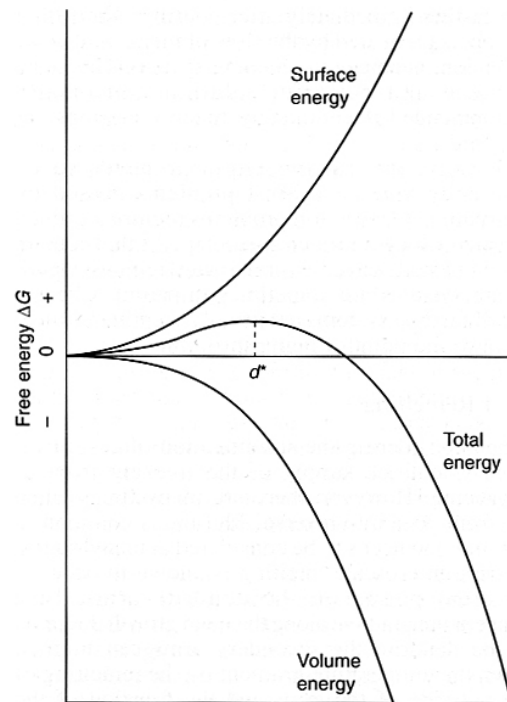
Figure 2-11 Maximum free energy and critical radius [8]

2.3.2 Heterogeneous Nucleation

Wetting is important for the contact between phases, mass transfer, and filtration and to describe nucleation and solidification phenomena. With heterogeneous nucleation, the energy of bubble formation decreases as a function of the wetting angle θ [8,19].

Fisher considers the case of the nucleation of a bubble against the surface of a solid substrate. The liquid is considered to make an angle θ with the solid. This contact angle defines the extent of wetting; θ=0 degrees means complete wetting, whereas θ=180 degrees is complete non-wetting. The geometry of a bubble in contact with a solid is shown in figure 2-12.

Fisher shows that nucleation is easier by a factor:

$$\frac{p_{het}^{*}}{p_{hom}^{*}} = 1.12[\frac{(2-\cos\theta)(1+\cos\theta)^{2}}{4}]^{\frac{1}{2}} \qquad\qquad 2\text{-}10$$

According to figure 2-13 Nucleation on solid surfaces does not become favorable until the contact angle exceeds 60 or 70 degrees. For this reason the nucleation of pores against the

growing solid such as a dendrite is not favored. This factor is contrary to those other factors that favor the nucleation of a pore close to a front. These favorable factors include the high gas contents and low surface tension usually present in the highly segregated liquid [7].
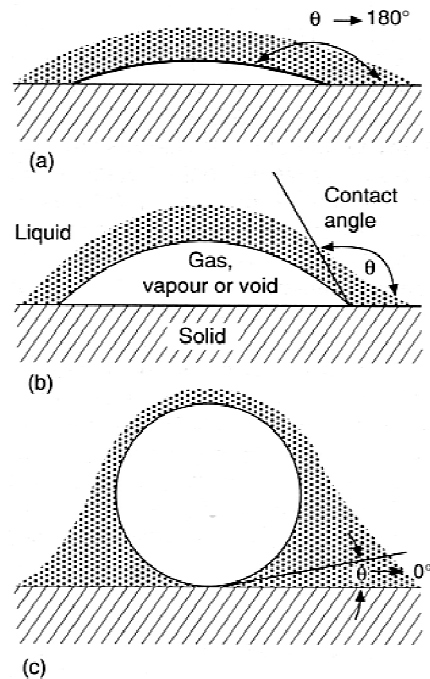
Figure 2-12 Geometry of a bubble in contact with a solid: (a) Poor wetting; (b) Medium wetting; (c) Good wetting, where cohesion of the liquid to the solid is high [7]

The wetting angle for solid-liquid combinations of aluminium and aluminium oxide are between 115° and 167° in the temperature range 704° C to 927° C [6]. Campbell [7] calculated that the required pressure for heterogeneous nucleation in an A356 type alloys was reduced to around 1500 atmosphere. Although the pressure required for heterogeneous nucleation is 1/20th of that of homogenous nucleation, it is still too high to be reached in a usual solidification process.
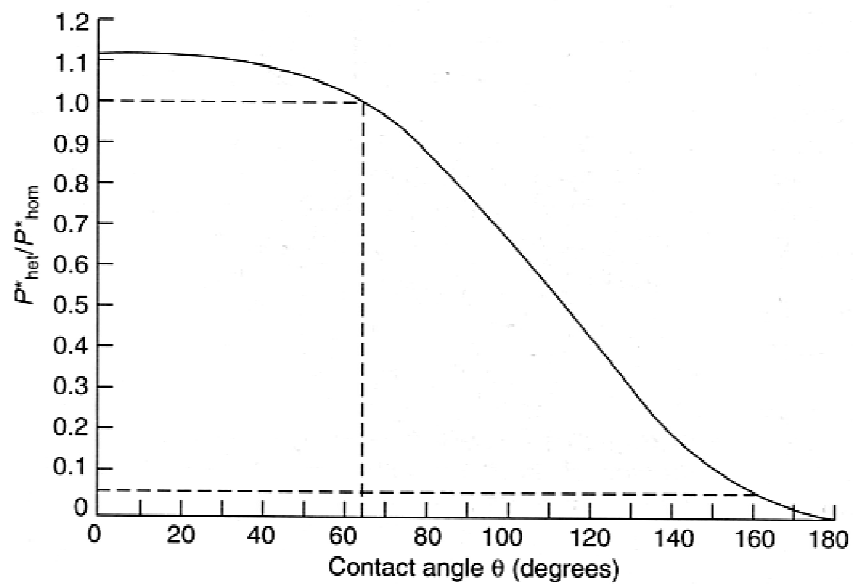
Figure 2-13 Relative difficulty of nucleating a pore as the contact angle with the solid changes from wetting to non-wetting [7]

2.4 The Concept of Surface Entrainment: Bifilms

It is worth mentioning that the alumina film, which forms on liquid aluminium, originally is not detrimental to the melt quality. The molten aluminium can actually benefit from this oxide skin, because, in fact, the oxide layer protects the melt from further oxidation. But the problem comes up when the surface film submerged and entrained in the melt, because of turbulence in the melt [7,10].

If the surface of the melt is folded in to the bulk of the liquid, the surface oxide is folded in, with its upper dry surfaces in mutual contact, as shown in figure 2-14. Accordingly, the entrainment mechanism can be defined as folding-in action that necessarily folds over the film dry side to dry side [14]. The submerged surface has to be necessarily double, since, as the piece of oxide is pushed through the surface of the liquid, the surface film on the liquid is automatically pulled down either side of the introduced oxide, coating both sides with a double film. These surfaces, being a solid, dry ceramic, stable, and cannot bond and it is termed as '*bifilm*'.
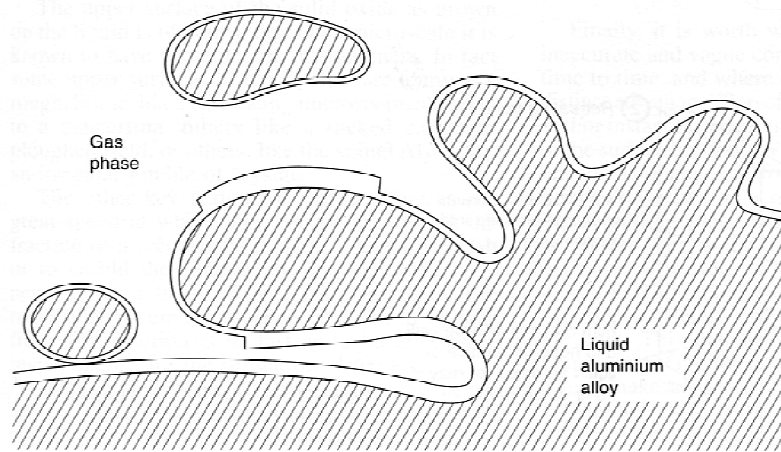
Figure 2-14 Surface turbulence; probably the most common mechanism of introducing bifilms into the melt [2,7]

The entrained piece of surface oxide always is double and some air is trapped in between two halves. This double surface oxide constitutes a defect that act exactly like a crack, because the negligible bonding across the dry opposed interfaces [2,7,14]. The cracks have a relatively long life, and can survive long enough to be frozen into the casting and can severely reduce mechanical properties.

Entrainment does not necessarily occur only by the dramatic action of a breaking wave; it can occur simply by the contraction of a 'free liquid' surface, as seen in figure 2-15. In the case of a liquid surface that contracts in area, the area of oxide itself is not able to contract. Thus the excess area is forced to fold into the melt.
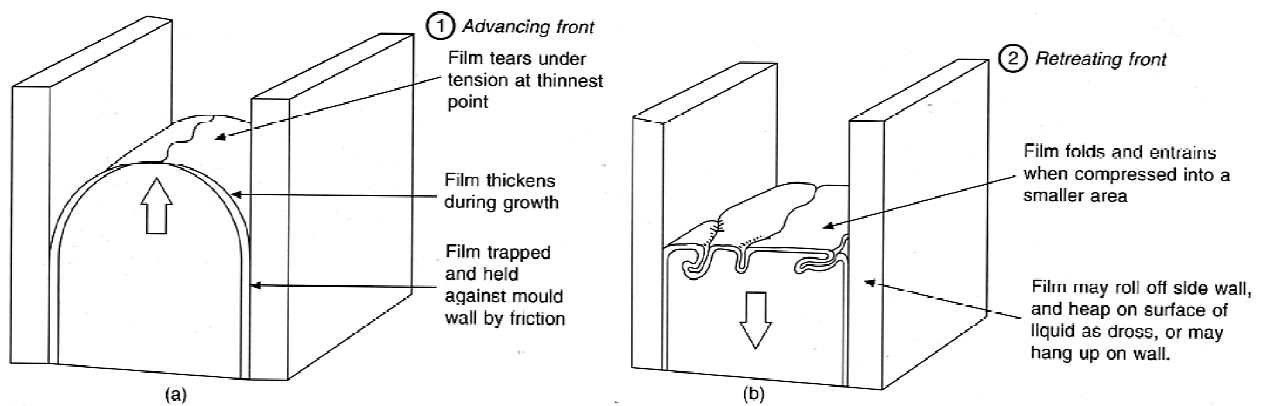
Figure 2-15 Expansion of the surface followed by a contraction, leading to entrainment [7]

When considering submerged oxide films, it is important to emphasize that the side of the film which was originally in contact with the melt will continue to be well wetted. Accordingly, it will adhere well, and be an unfavorable nucleation site for volume defects such as gas bubbles or shrinkage cavities. When the metal solidifies the metal-oxide bond will be expected to continue to be strong, as in the perfect example of the oxide on the surface of all solid aluminium products, especially noticeable in the case of anodized aluminium [7]. Figure 2-16 illustrates how entrainment can result in a variety of submerged defects.
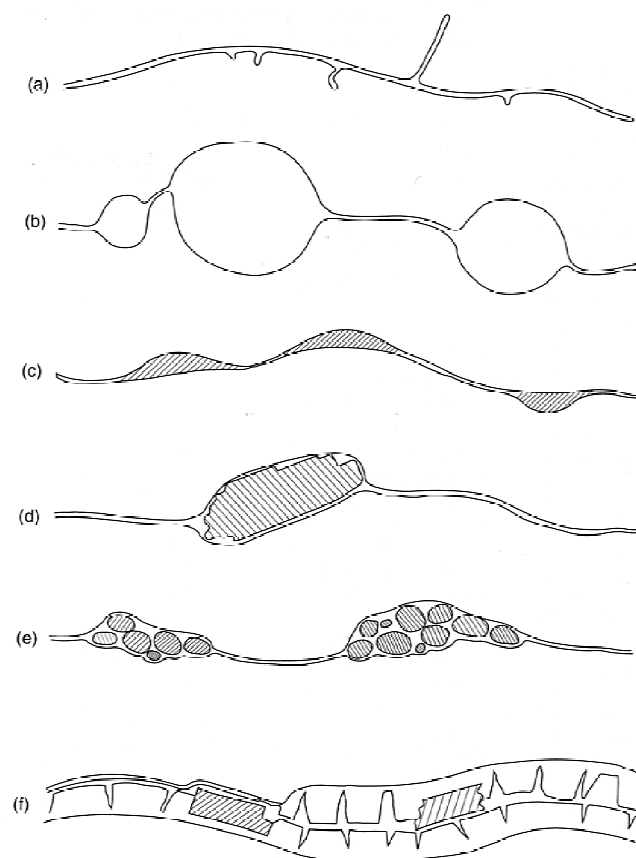
Figure 2-16 Entrainment defects: (a) a new bifilm; (b) Bubbles entrained as an integral part of the bifilm; (c) Liquid flux trapped in a bifilm; (d) surface debris entrained with the bifilm; (e) Sand inclusions entrained in the bifilm; (f) an entrained old film containing integral debris [7]

The figure 2-16a illustrates an entrained surface which caused a bifilm entrapment in the melt. It shows how an entrained film results in crack-like defects. When the turbulence in the melt forms a bifilm, pockets of air can be trapped in between the surfaces and this appears to be the most common source of porosity. However, the oxides are denser than liquid, but the

trapped air between the two halves of the film, causes a complicated behavior of oxides in liquid aluminium. The trapped air brings the density of oxide bifilms close to neutral buoyancy. Initially, enclosed air aids buoyancy and causing the films to float to the top surface of the melt. But, the enclosed air will be slowly consumed by the slow oxidation of inner surfaces of bifilm and it results in decreasing the buoyancy. There is a possibility that the bifilm can find a leak path connecting to the outside surface and allowing the bubble to deflate. These collapsed areas become an integral part of the original bifilm; figure 2-17 illustrates all steps of collapsing the bubbles.
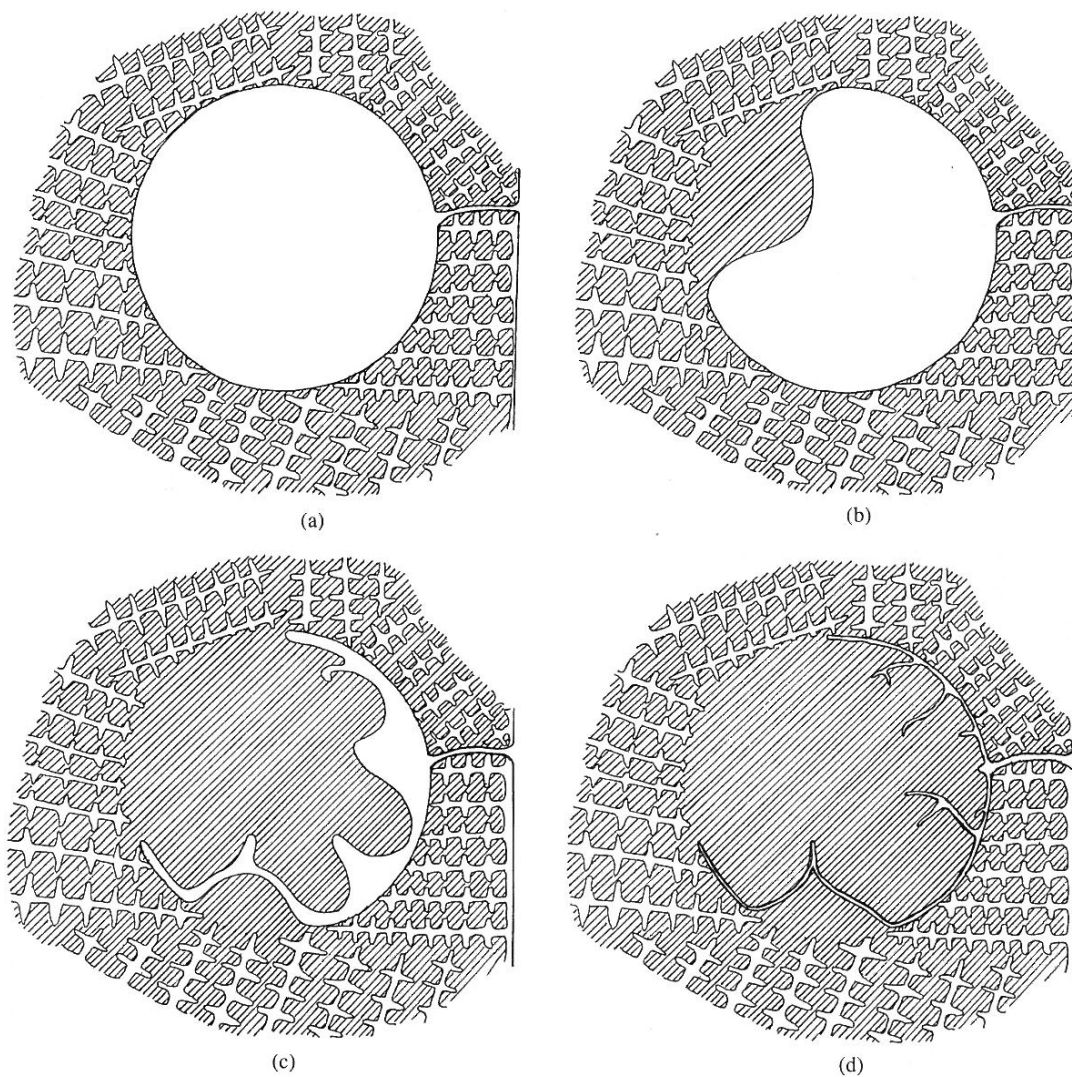

(a)

(b)

(c)

(d)

Figure 2-17 Schematic illustration of the stages in the collapse of a bubble [7]

2.4.1 Bifilm, Hydrogen and Porosity formation

Recently, it is recognized that hydrogen porosity cannot nucleate homogeneously and even heterogeneous nucleation of porosity is not possible. In contrast, the opening of a bifilm needs negligible force, being so easy that it can be assumed that this process will be overwhelmingly favored. Accordingly, for the initiation of porosity, whether gas or shrinkage, and whether in conditions that are well fed or unfed, or high gas or well degassed levels, it is assumed that bifilms are the initiation sources.

During solidification, hydrogen will be segregated ahead of the solidification front, and may exceed the solubility limit. Since hydrogen porosity cannot nucleate either homogeneously or heterogeneously, it is suspected that it remains in a supersaturated state. However, in the presence of a bifilm with its encapsulated film of air, the hydrogen can diffuse in and start to expand the bifilm to form a pore with negligible difficulty [14].

2.5 Furling and Unfurling of Bifilms

In the entrainment process bifilms forms, but they undergo many geometrical rearrangements. Internal turbulence of the melt is the main cause of these actions. The stages in the rearrangements of bifilms are:

- Entrainment by surface turbulence;

- Furling by bulk turbulence; and

- Unfurling in the stillness of the liquid metal after the filling of the casting is complete.

Under these circumstances, bifilm will be effectively deformed approximately 10 times in shape and size. They can change from a planar crack to a ragged ball shape as shown in figure 2-18a. Figure 2-18b, c show the stages and how a planar bifilm grows and change to bigger planar crack or pore.
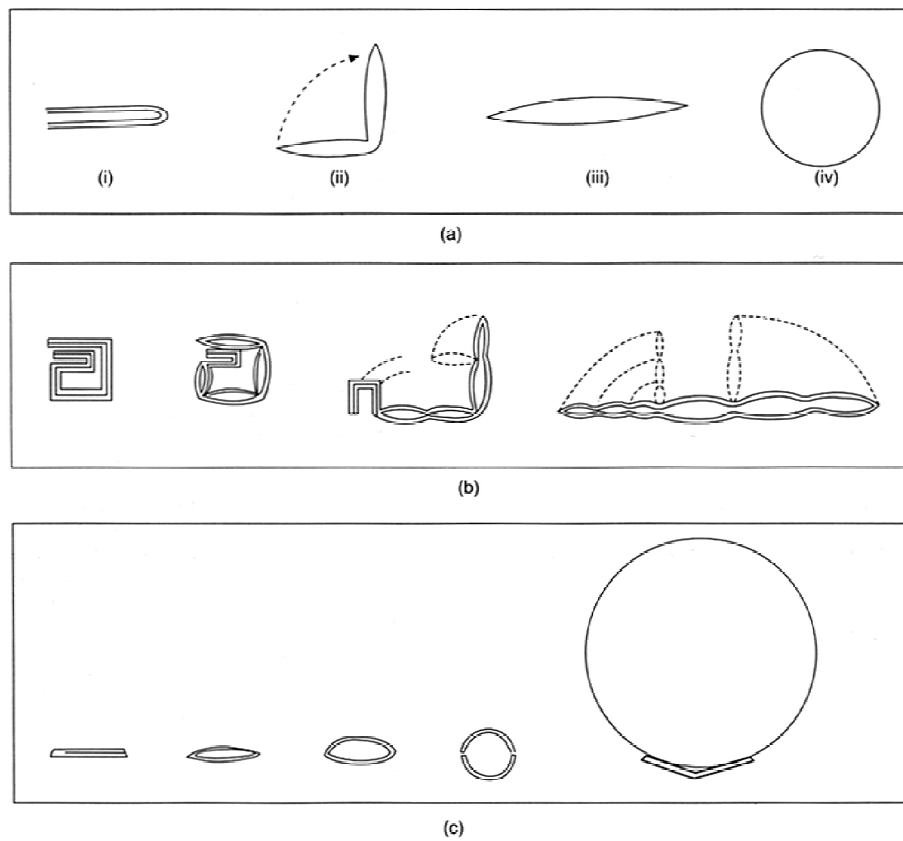
Figure 2-18 Stages of unfurling and inflation of bifilms [7]

On comparison, the compact and convoluted bifilms have a lower tensile strength than pores, because of the mechanical interlinking of the crumpled crack [7]. These mechanical interlocking of sound material can increase the plastic and shearing deformation. Because of the combination of this small strength with their small size, the compact bifilms are rendered as harmless as possible during furling stage, as is shown in figure 2-19.
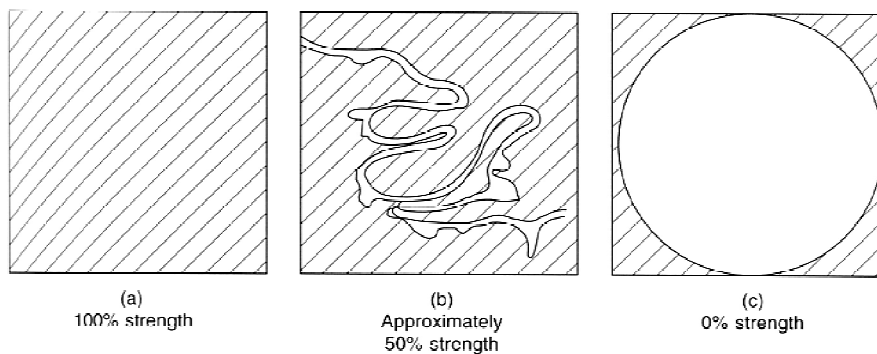
Figure 2-19 Relative strength (a) solid matrix, (b) Convoluted bifilms and (c) pores [7]

Based on rearrangement stages, on third stage, once the filling of the casting is complete, bifilms start to unfurl, opening, and growing to their initial form. By this action the defect now re-establish itself as a planar crack, and so can impair the strength and ductility of the metal to the maximum extent. There are several potential driving forces behind this phenomenon:

1. The precipitation by hydrogen in the gas film between the oxides interfaces, thus inflating the defect.

2. Shrinkage may pull the two films apart.

3. Iron rich phases nucleate and grow on the outer, wetted surfaces of the bifilm.

4. Oxides are pushed ahead of growing dendrites, effectively organized into planar areas among dendrite arrays, and are pushed into interdendritic and grain boundary regions [14]. The figures 2-20 and 2-21 illustrate the growing process of bifilms between dendrites during freezing between dendritic arms.
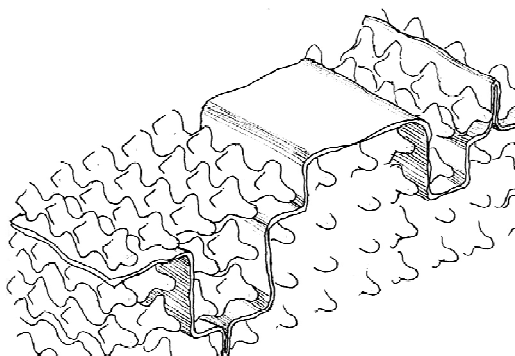
Figure 2-20 Schematic action of advancing dendrites to straighten a bifilm [7]
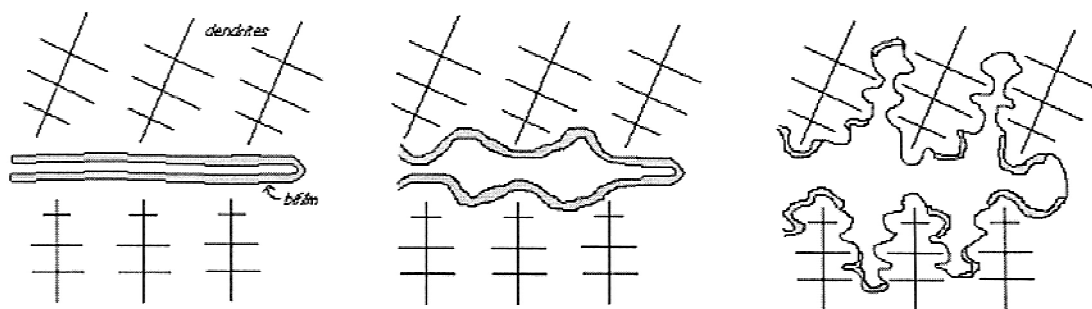
Figure 2-21 Stages of growing bifilms between dendritic arms [7,14]

28

Figure 2-22 is a flowchart of how defects like double oxide layers form and parameters which affect on the formation of these defects.
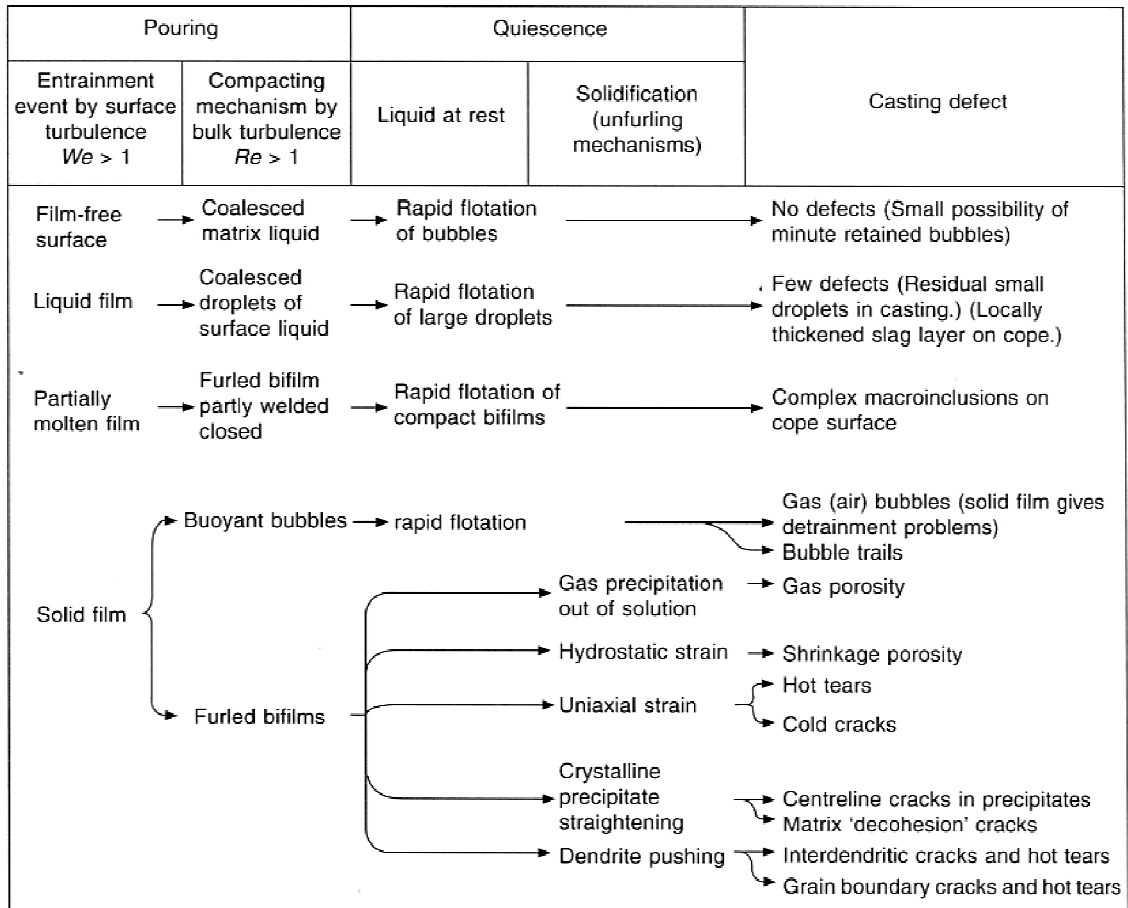
Figure 2-22 Framework of logic linking surface conditions, flow and solidification conditions to final defects [7]

2.6 Factors affecting the porosity formation in aluminium alloys

It is vital to investigate the problem of pore formation during solidification and the parameters which have effect on their formation [3].

It has been proven that [6,10] porosity formation in aluminium alloys is a mechanism of complex interaction of many factors such as, chemical composition, solidification range, volumetric shrinkage, cooling rate, heat extraction, melt quality.

2.6.1 Hydrogen Content and Cooling Rate

At low initial concentrations of hydrogen, pores form late and they are usually small. At high initial concentrations, pores start to form in the early stages of solidification and grow much larger. Four different types of pores, their development and characterization, in the bubbles are explained in figure 2-23.
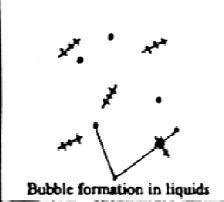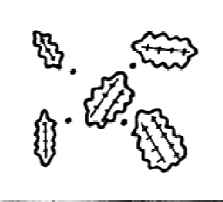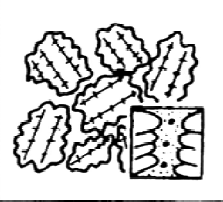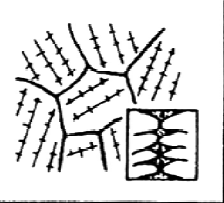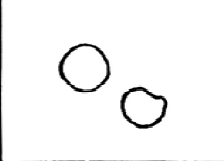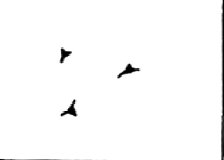
	1) round pores	2) long, broad pores	3) long, fissured pores	4) small, fissured pores
Solidification process and bubble formation	Bubble formation in liquids			
Pore morphology in the structure				

Figure 2-23 Four different types of pour morphologies. Hydrogen concentration increases from left to right [19]

Increasing the solidification rate reduces the time for diffusion of hydrogen into the bifilms and eventually, porosity will decrease [10,13]. Figure 2-24 presents the relationship between porosity, cooling rate and hydrogen content.
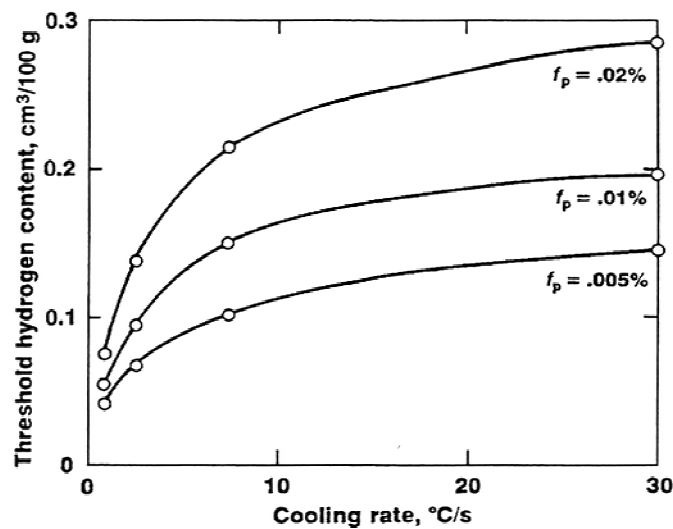
Figure 2-24 Relationship between hydrogen content, cooling rate, and porosity fraction, f_p [13]
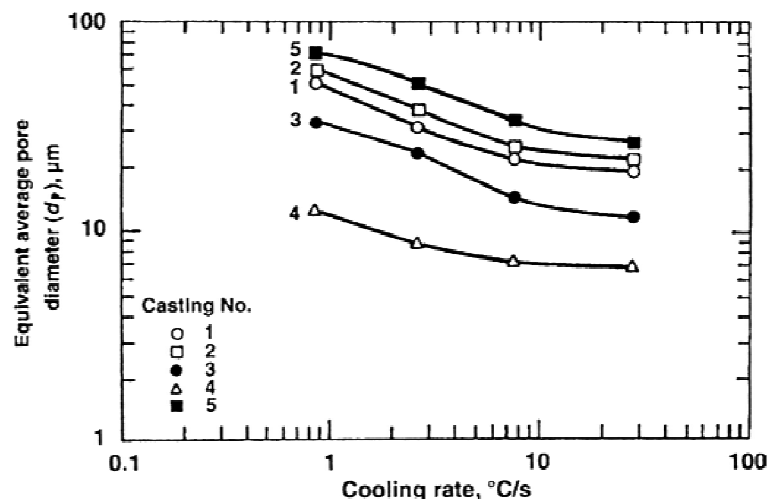
Figure 2-25 Relationship of pore size to cooling rate for different hydrogen content in alloy A356.0 [13]

It was found [7] that at short solidification time the pore density increased with increasing hydrogen content, according to figure 2-24. Figure 2-25 shows the comparison of five casting samples with different H_2 content and modifier, as shown in table 2-2. By comparing curve 4 and 5 in the figure 2-25 the higher H_2 content caused higher equivalent average pore diameter in casting. Furthermore, the grain refined castings in constant H_2 content shows smaller pore size in comparison with non-grained refined castings.

Table 2-2 Specification of samples in figure 2-25

Casting No.	H_2 Content (cc/100gr)	Specification
1	0.25	Non-grain-refined
2	0.31	Grain-refined
3	0.25	Grain-refined and modified
4	0.11	-
5	0.30	-

Conversely, at long solidification times the pore density decreased as hydrogen content increased. The bifilm will further inflate extra sections with time and additional concentration of gas. Figure 2-26 illustrates the relation between solidification time, pore density, and hydrogen content.
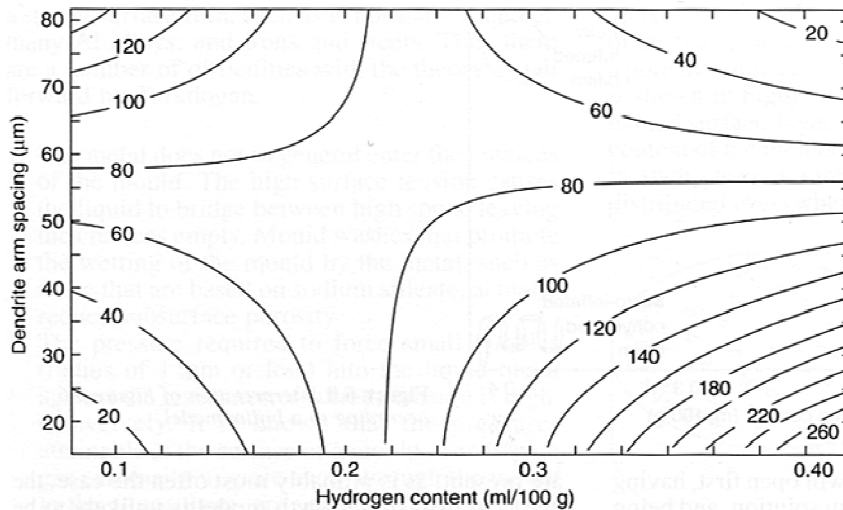
Figure 2-26 Pore density increases at fast freezing rates but decreases at slow freezing rates [7]

At low gas contents and short solidification times the bi-films remain folded and porosity is minimal. As the solidification times increases, the bi-films starts opening and gas porosity increases. At high gas contents and solidification times, large gas pores are formed with decreases in the pore number density. This result also explains that porosity-free casting does not necessarily mean bifilm free casting [6].
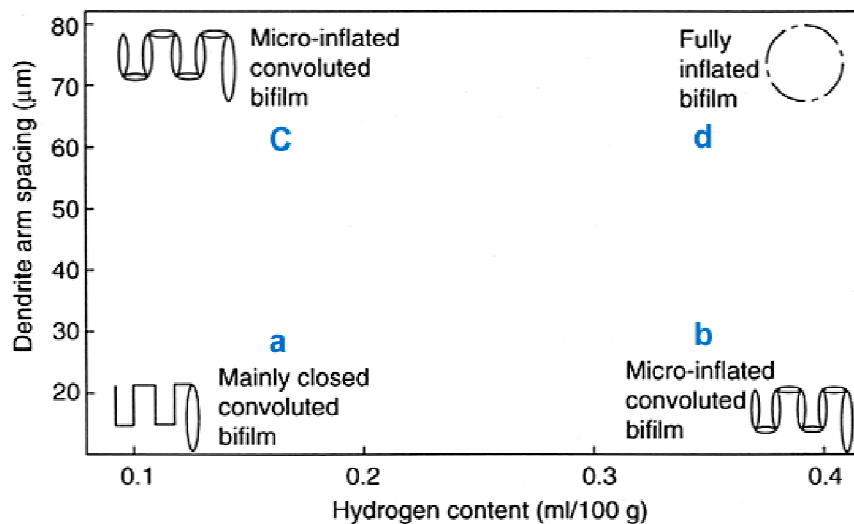
Figure 2-27 Interpretation of figure 2-26 according to a bifilm model [7]

a) High cooling rate and low gas content ………. Mainly closed bifilm.
b) Slow cooling and low gas content ………. Partially opened bifilm.
c) High gas content and slow cooling rate ………. Partially opened bifilm.
d) High gas content and slow cooling rate ………. Fully opened bifilm [6].

2.6.2 Grain refinement

Grain refiners are added to alloys to increase the strength and toughness by changing the microstructure, especially to a smaller grain size. Among the several advantages of grain refining, the primary one is an improvement in the amount and distribution of porosity and shrinkage in alloys that tend to form macroporosity. This results in a significant improvement in the mechanical properties of the casting, especially under fatigue loading, since fatigue in Al alloys is intergranular [3]. Grain refining also reduce the amount of porosity found in an alloy containing small or moderate amounts of gas [3,10].

The grain refiners tend to increase the number of dendrites and reduce their size. When the grain size is reduced, the size of the spaces available for pores to grow is also reduced and the consequence is a smaller pore size. Grain refinement not only limits the size of the pores, but it also leads to finer dispersion of porosity throughout the casting [20].

Grain refiners, such as Al-Ti and Al-Ti-B master alloys, are added in small amounts to molten Al alloys to control the grain structure in castings. $TiAl_3$ and TiB_2 particles act as nucleating sites for the formation of primary α–aluminium dendrites and promote a uniform and fine equiaxed structure [3,21- 25].

2.6.3 Melt Cleanliness

Commercial aluminium and its alloys contain broad range of inclusions in small quantities [26]. The content of the entrained inclusions is one of the foremost important factors, which affect on melt quality. Because the non-wetted surfaces constitute the initiation site for hydrogen diffusion and pore growth [27]. The main inclusions that occurs during melting or holding periods prior to casting are aluminium oxide (Al_2O_3), aluminium carbide (Al_4C_3), magnesium oxide (MgO), spinel ($MgAl_2O_4$), titanium diboride (TiB_2), aluminium boride (AlB) and titanium aluminide ($TiAl_3$) [28].

RPT experiments produced many important results and show the difference between filtered and unfiltered melts [27]. Castings produced from unfiltered melts contain a

significantly higher number of pores than in filtered castings. For example, filtration of the A356 melt alloy lowers the pore density as figure 2-28 illustrates this effect [27].
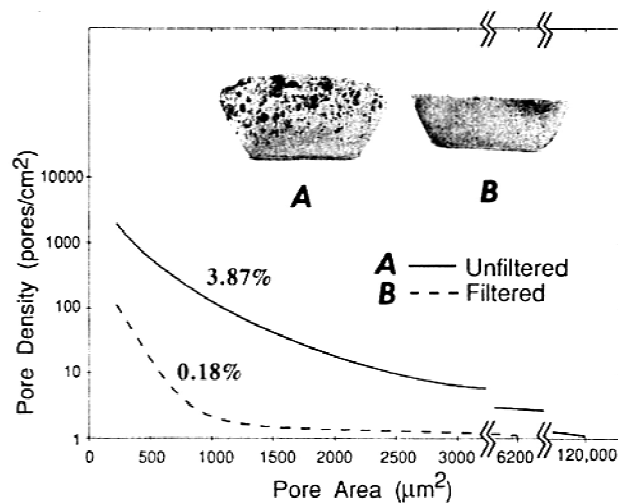
Figure 2-28 Pore distributions in A356 castings for filtered and unfiltered castings produced from dirty melt [27]

2.6.4 Melt Handling

Turbulence is the main reason of entraining bifilms in the bulk of the liquid during melting, holding furnace, and pouring into ladle or mould. During the pouring of liquid aluminium, the surface film on the liquid grows so quickly that it forms a tube around the falling stream. Campbell calls this an oxide flow tube [7]. When the melt is falling from greater heights, a large number of bifilms are incorporated into the melt resulting in detoriation of melt quality. Figure 2-29 illustrates the effect of height on oxide flow tube and pore morphologies at different pour height are shown in figure 2-30.
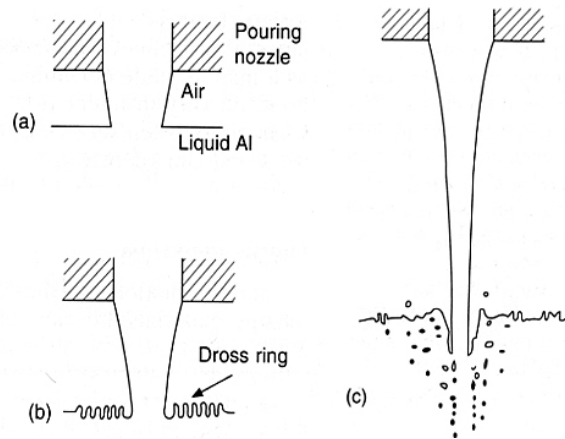
Figure 2-29 Effect of increasing height on a filling stream of liquid: (a) the oxide flow tube; (b) the oxide flow tube forms a dross ring; (c) the oxide film and air being entrained in the bulk liquid [7]

Arrangement of the pouring lip of the ladle in order to be as close as possible to the pouring cup of the mould causes protection against contact with the air [7]. This arrangement can reduce the oxide content on the surface or around the falling stream, therefore less bifilm will be formed by turbulence during pouring. It worth mentioning that minimization of turbulence at pouring or tapping step is considered required parameter to minimize the amount of trapped oxide in the bulk.
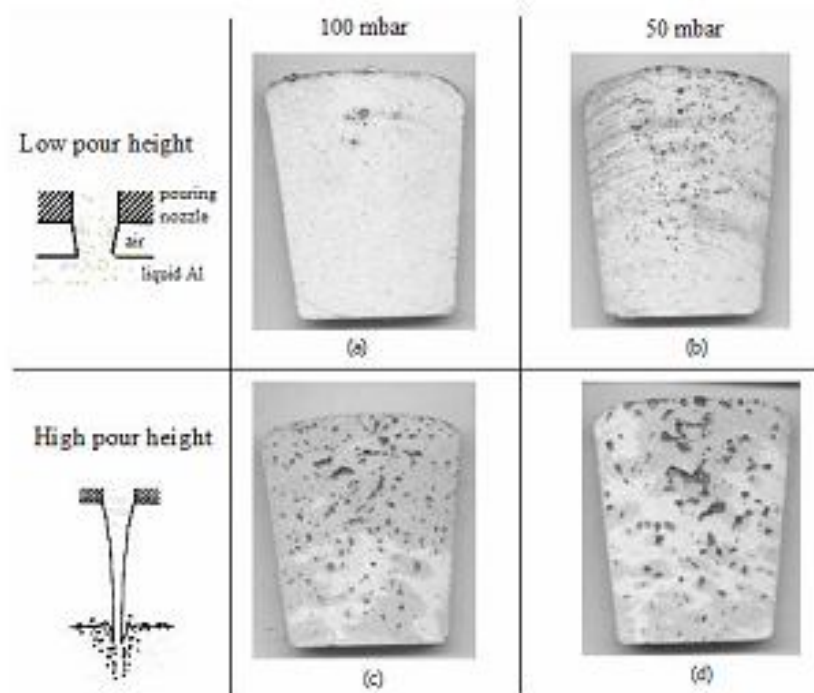
Figure 2-30 Different pore morphologies at different pour heights and vacuum levels [14]

2.6.5 Modification

A modifier is weighed in terms of its role in enhancing the susceptibility to hydrogen pickup of the modified alloy and changes its porosity content, in turn, it increases elongation and tensile strength in Al-Si foundry alloys [3].

Shahani [29] found that addition of Sr or Na actually reduced the gas content, although it increased the porosity of the modified casting. According to him, modifiers promote shrinkage porosity, facilitating the nucleation of pores by reducing the surface tension or by acting as nucleants.

Argo and Gruzleski [30] have carried out a controlled study on porosity in modified and unmodified A356 alloy, using the Tatur test to identify differences in the distribution of porosity and shrinkage. Their results have shown that modification leads to a redistribution of porosity on solidification, from primary pipe type into microporosity, appearing thereby to 'increase' the porosity.

Argo and Gruzleski [30] and Fang *et al.* [31] have observed that micropores in modified alloys are bigger. In unmodified alloys, the eutectic exhibits an irregular solid/liquid interface, because of which small pockets of liquid are entrapped between advancing solidification fronts, resulting in fine concentrated microporosity. But a regular and planar interface in modified alloys results in a more widely dispersed and larger porosity [3].

2.6.6 Effect of Iron

Iron is the most common and detrimental impurity present in aluminum casting alloys and has long been associated with an increase in casting porosity [32]. Some specifications of Iron cause these deleterious effects on the cast aluminium properties:

- Iron cannot be economically removed and it exists as an impurity in cast aluminium alloys.

- The solubility of iron in molten aluminium is quite high; In contrast, the solubility of iron in solid aluminium is very low.

- Fine Fe-rich intermetallic phases precipitate at intermediate temperatures and cannot be redissolved in the solid state, β-Al_5FeSi phase [33].

A number of Fe-rich intermetallic phases have been identified in Al-Si casting alloys, but the β phases was reported to be particularly deleterious to the castability and mechanical properties. The Platelet-shape of this phase is expected to cause severe feeding problems during solidification, and eventually to increase the tendency to porosity formation. The precipitation of coarse β platelets at high iron contents physically blocks the flow of the feed liquid in the interdendritic regions and this result in increase in porosity. The length and size of this intermetallic phase increase with an increasing iron content and decreasing cooling rate. Table 2-3 summerizes various parameters of modifying the Fe-rich phase efect [32-34].

Table 2-3 Parameters can affect on β-Al5FeSi phase formation [32]

Parameters	Possible effects
Fe	Change precipitation sequence of β
Mn, Cr, Be, Ni	transform β into α, but increase the total amount of Fe-rich intermetallics
Mg	transform β into π
P	promote the nucleation of β
Sr	dissolution, fragmentation, and even decomposition (at extremely high levels) of β
Cooling rate	low cooling rate generally favors the formation of β
Melt Superheating	refine and reduce the Fe-rich intermetallics including β and avoid sludge formation

2.7 Effects of Porosity and oxide films on mechanical properties

There are four factors that influence the mechanical properties [36]: composition, heat treatment, solidification rate, and integrity of the cast structure.

Porosity is a major cause in the reduction of mechanical properties, particularly elongation and fatigue resistance [34]. Interdendritic porosity after solidification is flattened into planar discontinuities under metal working condition. In thick plates and forgings, this leads to a reduction in the mechanical properties in the direction normal to the direction of working.

The presence of increased porosity in modified castings can easily offset the enhancement in their mechanical properties. The porosity induces tensile transverse stresses in Si particles and at the particle-matrix interface, which can promote crack initiation and, thus, lower the mechanical properties [37]. Porosity levels above 1% can significantly reduce the properties, especially % elongation. Figures 2-31 and 2-32 show the effect of porosity on tensile and yield properties.
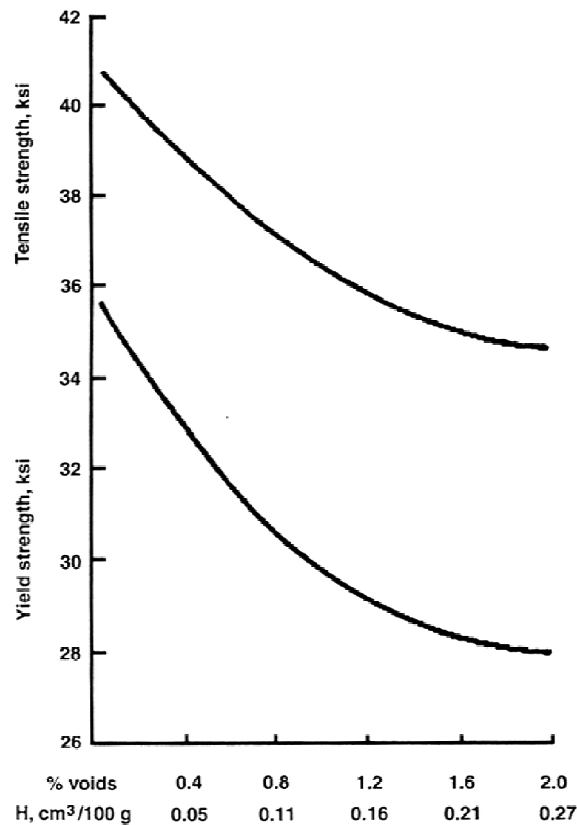
Figure 2-31 Effect of hydrogen porosity on the tensile and yield strength of alloy 356.0-T6 sand castings [13]

The oxide film formed on the surface of molten aluminium alloy can be entrained into the melt by surface turbulence, frozen into castings, forms *bifilm* and acts as a crack after solidification.

About the bifilms, their size, orientation, density on a cross-section, or all factors together, in a highly stressed region, can determine the mechanical strength. The presence of a bifilm in a stressed region can affect on mechanical properties because the bifilm may be opened by the stress [7].

Furthermore, the increase in oxide film defect sizes is important and can dramatically decreases the mechanical properties of castings [38]. Oxide films are also thought to be the initiator of fatigue cracks in the casting [39].
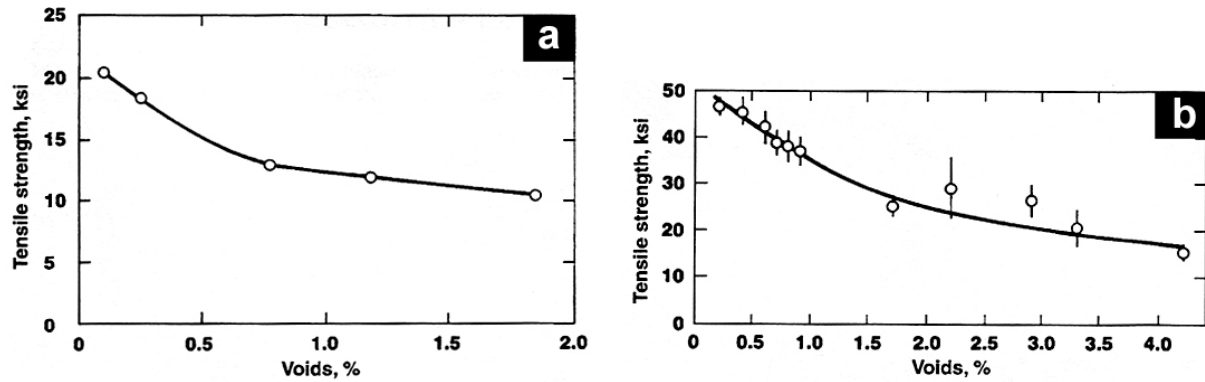

Figure 2-32 Effect of void content on the tensile strength of 2 selected aluminium alloy: (a) alloy 443.0-F; (b) alloy 520.0-T4 [13]

3 Experimental Procedure

This study was aimed to investigate the interaction between oxide and hydrogen and their effect on porosity formation. The experiments were designed to find out the effect that different level of oxides has on the porosity formation and distribution, while the hydrogen content is constant.

3.1 Alloys

The alloy used in the experiments was an A356 alloy. Two different melts were produced by making a change in oxide content. In order to increase the oxide content, two different kinds of addition, i.e. anodized plates and extruded aluminium oxide rods, were added to the molten alloy. The following shows the composition of each melt:

- **Melt 1:** A clean A356 melt, no additions of any particulates, has been used as reference material;

- **Melt 2:** Addition of 5% anodized and lacquered plates;

- **Melt 3:** Addition of 5% extruded aluminium oxide rods directly to the melt.

The melting experiments were conducted in an electric resistance furnace under carefully controlled conditions and the casting temperature was 750° C. Once the correct hydrogen level and temperature were achieved, the alloy was carefully poured into the sand moulds to produce different set of samples.

3.2 Hydrogen Measurement

To investigate the effect of different amount of oxide, the amount of hydrogen has been kept constant. First, the temperature has been increased up to 750° C and then the hydrogen level was measured by ALSPEK* H. The amount of hydrogen for each melt has been measured 0.24-0.25 ml/100gr for each melt.

Figure 3-1 ALSPEK H probe and its analyzer [39]*

ALSPEK* H is a device for the direct measurement of hydrogen concentration in aluminium alloys, as shown in figure 3-1. It is built around an electrochemical sensor, which is mounted in a probe constructed. The sensor is immersed in aluminium and the signal is processed by an analyzer and displayed as hydrogen concentration in ml/100gr [40].

3.3 Density Measurement

Samples have been produced from each melt under the same conditions. From each melt, 4 rods have been produced and each rod was cut to 5 pieces, according to figure 3-2. The density of 60 pieces was calculated by *Archimedes method*, according to equation 3-1.
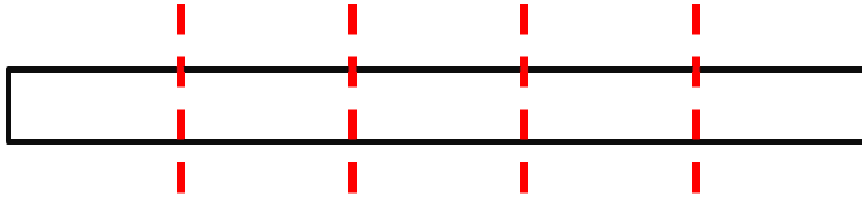
Figure 3-2 Casting rods were cut to 5 pieces and have used in density measurements and image analysis experiments

$$d = \frac{m_{air}}{(m_{air} - m_{water})d_{water}}$$ 3-1

d = Density of sample

m_{air} = Weight in air

m_{water} = Weight in water

d_{water} = Density of water

After calculating the density of each piece of samples, the volume percentage porosity of each melt has been calculated, according to equation 3-2:

$$d_{volume\ percentage\ porosity} = \frac{d_{sample} - d_{pure\ metal}}{d_{sample}} \times 100$$ 3-2

Density of samples was calculated from previous relation and density of pore free alloy is considered 2.678gr/cm^3. Thus, by this technique, the densities of each sample bar and finally the volume percentage porosity from each melt have been calculated.

3.4 Reduced Pressure test (RPT)

Reduced pressure test is an easy, robust, simple, low cost, relatively quick test that measured the effect of detrimental defects, hydrogen and inclusions, or mainly bifilms. It helps to achieve a semi-quantitative method to assess the melt quality, based on total length of bifilms. The following figure illustrates the basic concept of reduced pressure test.
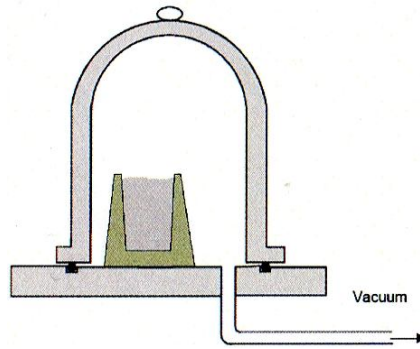
Figure 3-3 Basic concept of reduced pressure test

The equipment consists of a vacuum chamber and rotary pump. In each experiment and from each melt, six RPT samples were produced. Samples solidified under the same conditions, time and vacuum pressure. When the vacuum is applied in the RPT, the volume of air or other gases such as hydrogen, trapped inside the bifilm will expand; forcing the bifilms to become unraveled, and therefore opening and straightening with time. The mould and the sample which are produced in this technique are shown in figure 3-4.
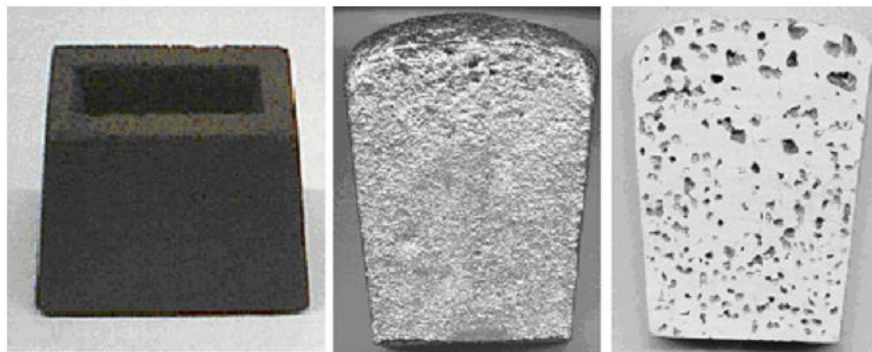

Figure 3-4 A RPT mould; a cast sample; a RPT sectioned sample [14]

Each sample was poured at 750° C and solidified under vacuum for 3 minutes. The sectioned surface of reduced pressure test samples were scanned and analyzed by '*SigmaScan software*' to calculate the sum of the maximum length of the pores, '*bifilm index*'.

$$Bifilm\ index = \sum (pore\ length) \qquad\qquad 3\text{-}3$$

'*Bifilm index*' was proposed as a quantifying concept and it gives a practical measurement of two important factors, the quality of the melt and total number of bifilms [1-2]. The RPT moulds and samples which have been used in this experiment are shown in figure 3-5.
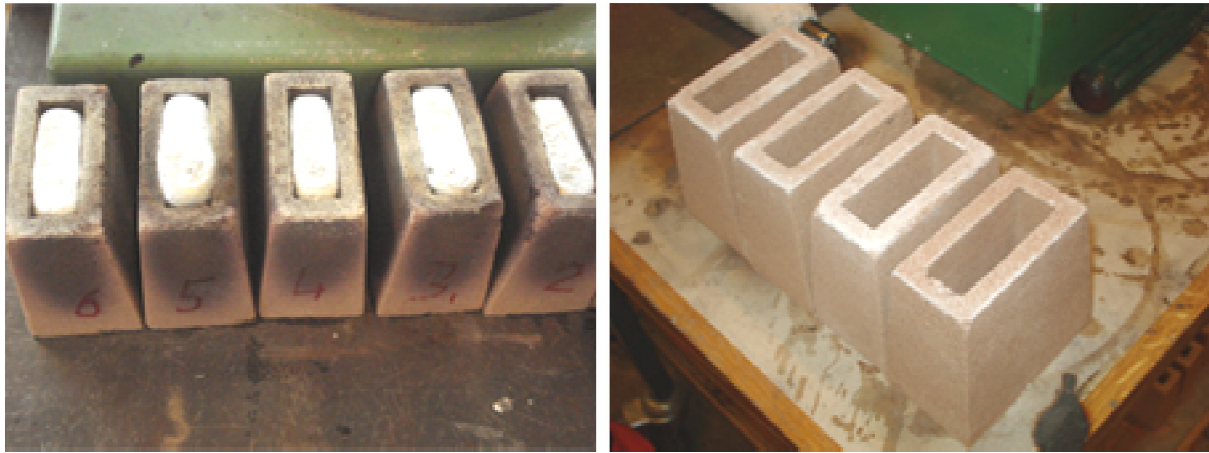

Figure 3-5 RPT moulds and final cast samples

3.5 Porous Disc Filtration Apparatus (PoDFA) Test

"PoDFA (Porous Disc Filtration Apparatus) is a method of metal cleanliness evaluation that provides both qualitative information on the nature of inclusions and quantitative information on the inclusion concentration [41]". Figure 3-6 illustrates the principal of PoDFA operation.

This method contains two main steps, sampling and metallographic analysis. In the first step, a predetermined amount (1.5 kg) of liquid aluminium is poured into a preheated crucible. A very fine porosity filter is fixed under the crucible and the melt is sucked from the crucible under controlled conditions. Inclusions in the melt are concentrated at the filter surface by a factor of about 10,000.
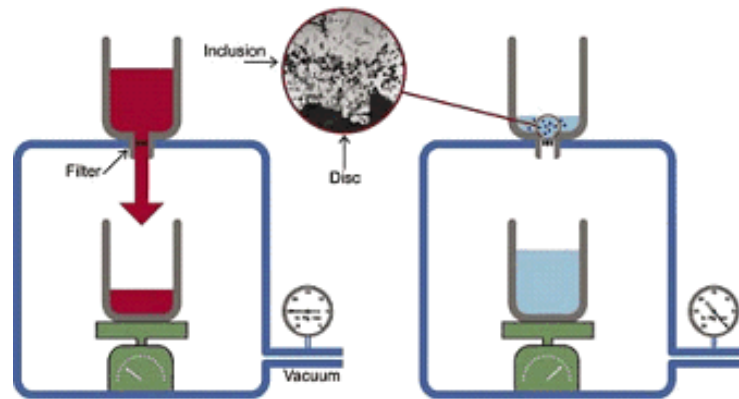
Figure 3-6 PoDFA principle of operation [40]

Three PoDFA samples were produced from each melt for quantitative evaluation of the present inclusions. The filter with all inclusions and impurities, is cut, mounted, and polished. The final sample is used for metallurgical and microscopic analyses. PoDFA instruments, crucible, and filters are shown in figure 3-7.

Figure 3-7 PoDFA instruments [40]

3.6 Bending Test

Bend Tests are conducted to determine the ductility of a material. The maximum stress at fracture is referred to as the *bend strength* or the *modulus of rupture* [42]. To calculate the maximum stress, the three-point bending test set-up was used. It consists of a mandrel and two specimen supports. The sample fixed on the bottom supports without any further support. The distance between these two supports is fixed regarding the mandrel radius, *d*, and thickness of sample; *h*. Bending force is applied at the center of the specimen, by mandrel. The drawing of the bending test instrument is shown in figure 3-8.
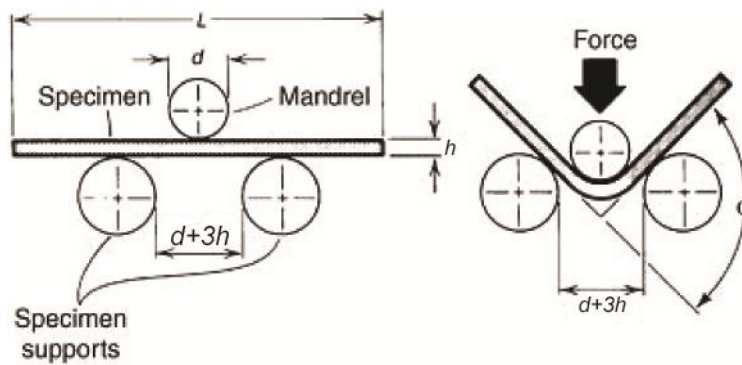
Figure 3-8 Principle of 3-point bending test [42]

Three parallels of bending samples were produced from the melts and they were machined with dimensions 70×10×3 mm. Four bend samples from each parallel were machined and in total bend testing was carried out for 12 samples from each melt. Figure 3-9 shows the schematic diagram of bending test mould.
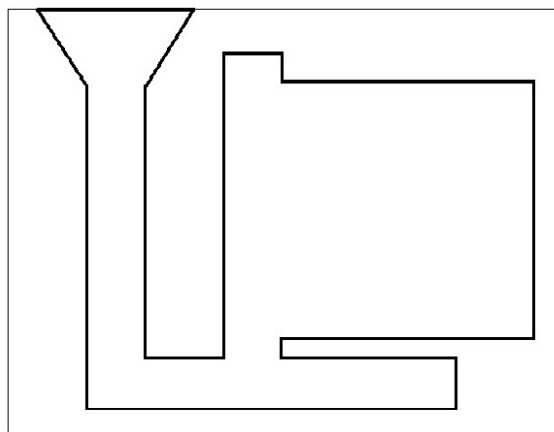

Figure 3-9 Schematic diagram of bending test piece moulds

The maximum stress at fracture was measured by the bending device and modulus of rupture has been calculated by equation 3-4, the average maximum fracture stress at fracture and the bend strength of each group of samples will be compared. Figure 3-10 shows the three-point test stress distribution and the sample parameters.

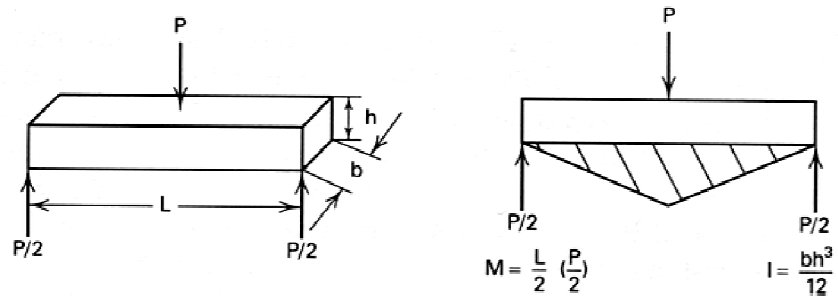$$\sigma_{3-pt} = \frac{3PL}{2bh^2}$$
3-4

Figure 3-10 3-point bending stress distribution [42]

3.7 Tensile Test

The uniaxial tensile test is a method to investigate the stress-strain behavior of materials. Specimen has to be machined and formed according to figure 3-11. Then the specimen is mounted into a mechanical testing machine, as shown in figure 3-12, where it elongated with constant crosshead speed (1.5 mm/min), and both the elongation Δl and the applied force F are continuously recorded.
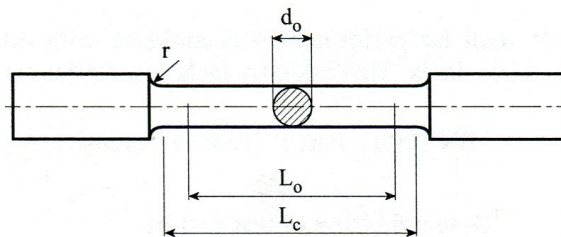

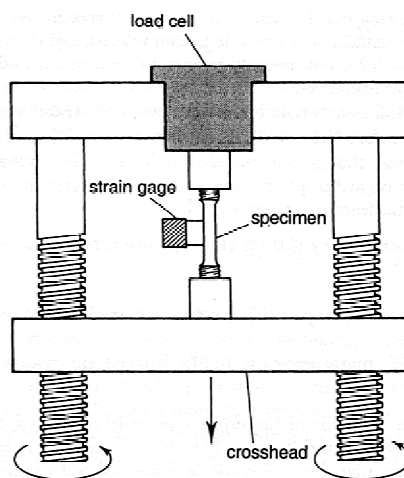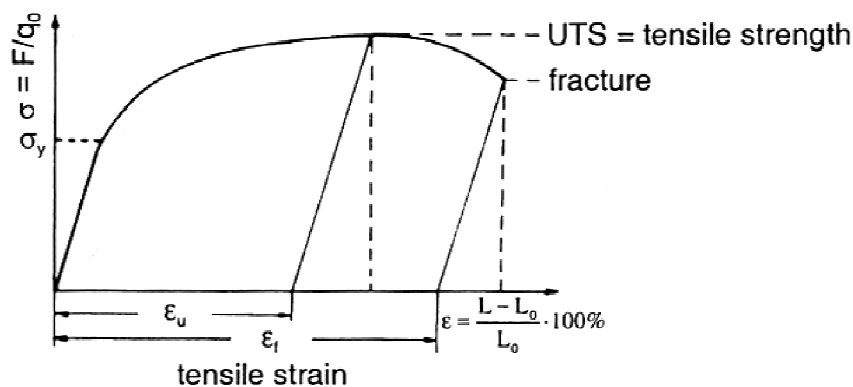*Figure 3-11 Machined tensile sample*

Figure 3-12 The principle of dynamic tensile test [44]

It is common to define several strength levels that characterize the material's tensile response. Although, diagrams vary greatly in detail, the essential features of the diagrams are common. After exceeding a yield stress σ_y, stress level related to the onset of irreversible plastic deformation, the stress gradually increases with strain until maximum UTS (ultimate tensile strength). The ultimate tensile strength is defined as the maximum load divided by the initial cross-sectional area. Figure 3-13 shows a schematic stress-strain diagram and the important characteristic quantities of materials.

Figure 3-13 Schematic engineering stress-strain diagram showing the important characteristic quantities of materials [44]

Two parallels of tensile sample moulds were produced from each melt, and in total 20 samples for each melt were machined and prepared, according to the figure 3-11. The drawing of moulds that have been used to produce samples is shown in figure 3-14.

The uniaxial tensile test has been done on all 60 samples and stress-strain diagram was plotted for each sample. From each group of samples, some fracture surfaces were selected for SEM analyses.
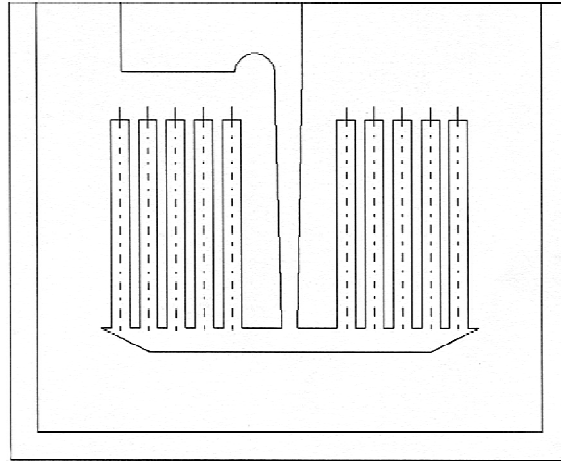
Figure 3-14 Schematic diagram of tensile test piece moulds [1]

3.8 Image analyses

The samples which have been used in density measurement were mounted and prepared for image analyses. First of all, samples were mounted, ground, and polished. They were ground by 80 to 4000 grade SiC papers, and then were polished by 3 µm and 1µm MD-Nap plate. The surface of each sample was scanned by a light microscope with a magnification of 2.5 x. The images were digitized, calibrated, and analyzed by image analysis software. *ImageAccess (easylab 6)* software has been used in this study and the results are reported in terms of shape factor, pore size distribution, and average diameter of porosities.

3.9 Scanning Electron Microscopy

The scanning electron microscope (SEM) uses a high energy, focused beam of electrons to generate a variety of signals at the surface of solid specimens. The types of signals derive from the electron-sample interactions include secondary electrons, backscattered electrons, characteristic X-rays, and transmitted electrons. These signals contain information about the sample's external morphology (texture), chemical composition, and crystalline structure and orientation of materials making up the sample. Features seen in the SEM image may then be immediately analyzed for elemental composition using EDS or WDS [45,46]. The principle of Scanning Electron Microscope is shown in figure 3-15.

The fracture surfaces of some samples have been analyzed by electron scanning microscope in order to investigate the pores, oxides, and their effect on fracture. The samples were produced from fracture surfaces of tensile test samples. From each group, the samples with maximum and minimum fracture strength were selected and analyzed by SEM.
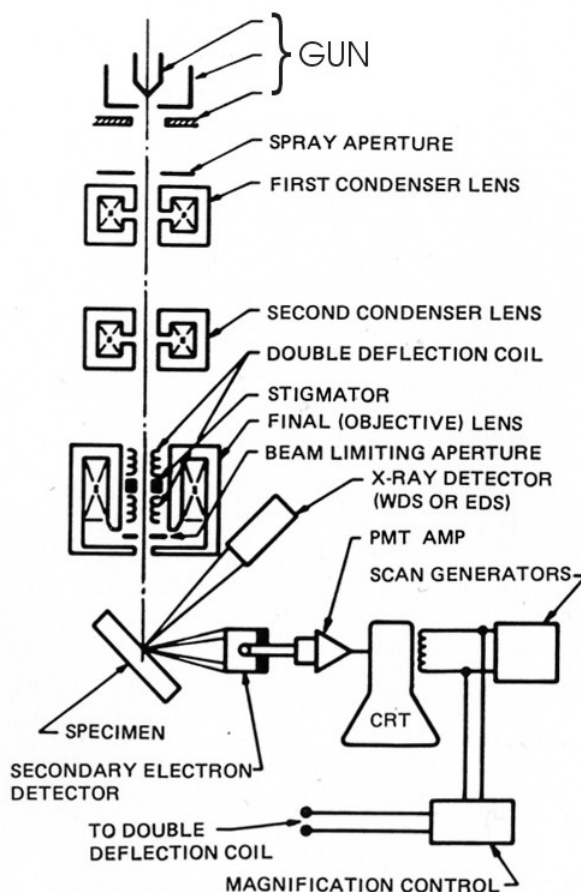

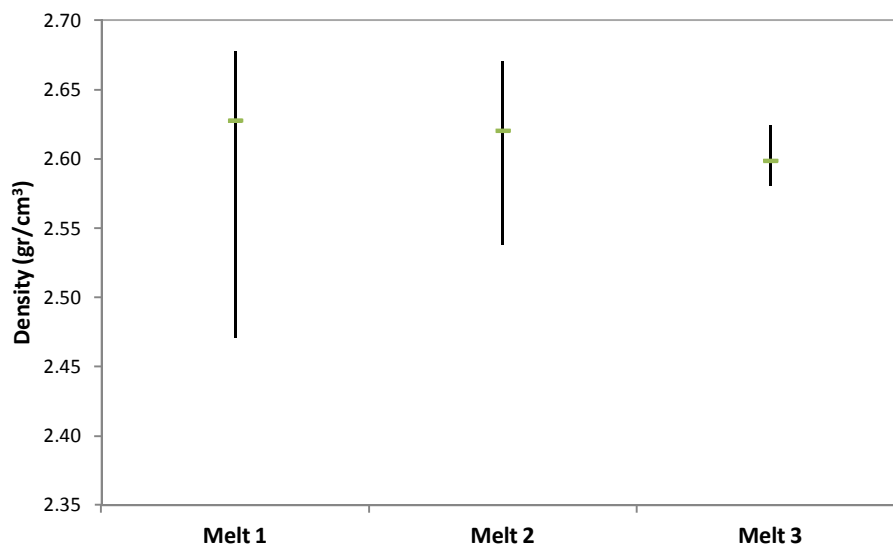*Figure 3-15 Principle of SEM [45]*

4 Results and Discussion

This chapter presents the quantitative results and measurements with a comprehensive discussion about important findings.

4.1 Density Measurement

The following results have been produced by Archimedes method and show the average density and volume porosity percentage from each melt:

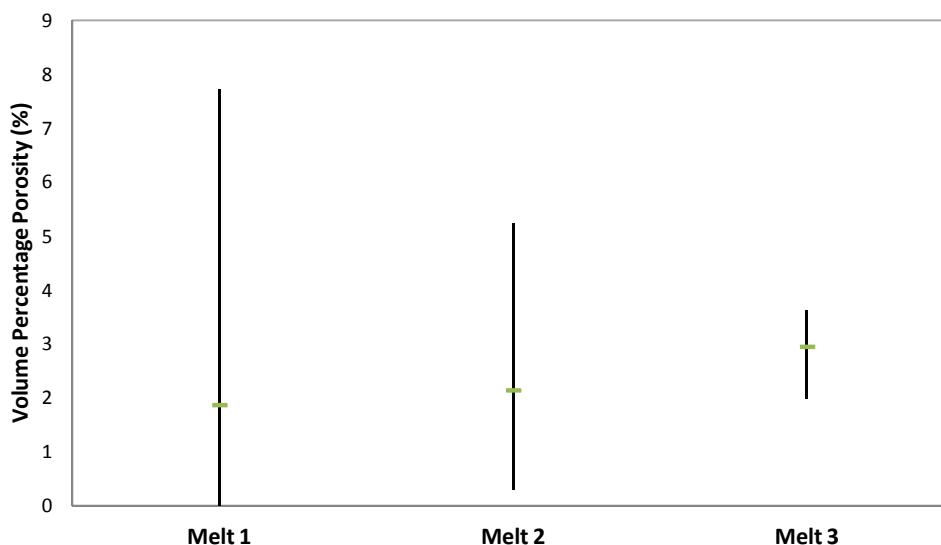*Figure 4-1 Average density of samples from each melt*

Figure 4-2 The comparison of average Volume percentage porosity of each melt

The average density measurement of 48 samples collected from three different melts is given in figure 4-1. Furthermore, the average volume percentage porosity is calculated by equation 3-1 and the results are presented in figure 4-2 and table 4-1.

	Table 4-1 Density of each melt				Table 4-2 Volume percentage porosity of each melt		
	Max.	Min.	Ave.		Max.	Min.	Ave.
Melt 1	2.68	2.47	2.63	Melt 1	7.72	0.01	1.87
Melt 2	2.67	2.54	2.62	Melt 2	5.23	0.29	2.14
Melt 3	2.62	2.58	2.6	Melt 3	3.63	1.99	2.95

The results and figures show the effect of additions on porosity formation in each melt. Figure 4.2 shows a slight increase in volume porosity by adding anodized plates and oxide rods. Reference melt had the lowest volume percentage porosity and third melt had the highest amount of porosities.

Furthermore, density measurements indicate that there is a relationship between density of the sample and volume porosity percentage. Figure 4-3 shows that with increase in porosity density is lower.
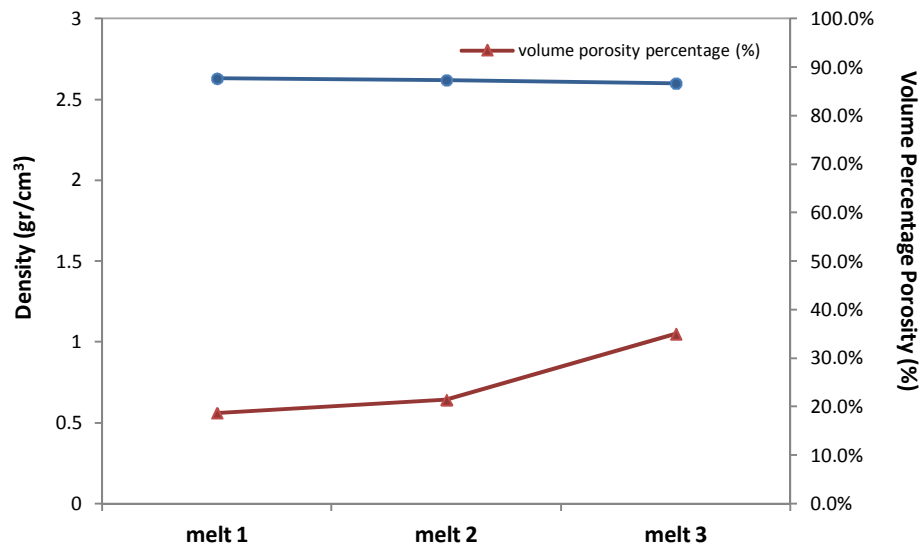
Figure 4-3 Comparison of density and volume percentage porosity

4.2 Reduced Pressure Test

The total length of bifilms, *bifilm index*, estimated from sectioned surface of reduced pressure test samples, using the *SigmaScan* and equation 3-3. The sectioned surfaces of one example of each of the series of RPT experiments are shown in Figure 4-4.
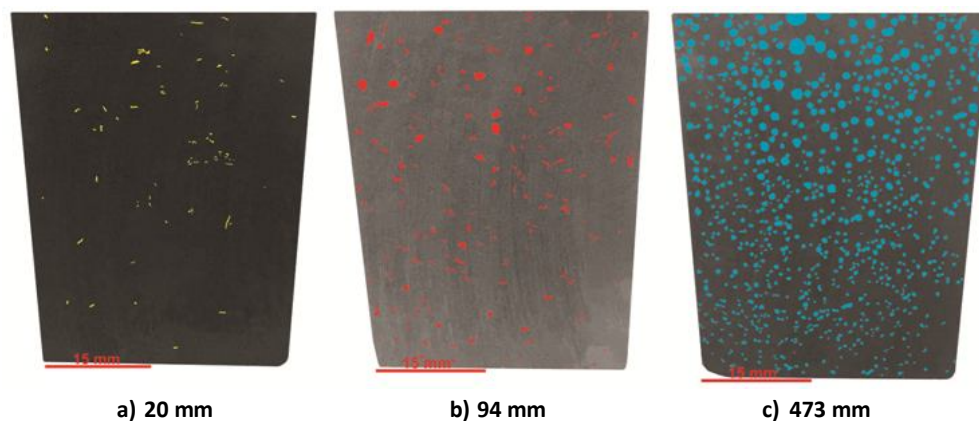

a) 20 mm   **b) 94 mm**   **c) 473 mm**

Figure 4-4 Sectioned surfaces of RPT samples after analyzing: a) melt 1; b) melt 2; c) melt 3

The number of pores of the RPT samples shows an explicit decrease of the melt quality by addition of anodized plates and oxide rods. Bifilm index was lower in melt 1, but the pores formed in other melts when the oxides were deliberately introduced with results in higher

bifilm index values. The average bifilm index comparison of samples of second and third melt obviously shows that melt 3 contains higher amount of bifilms.
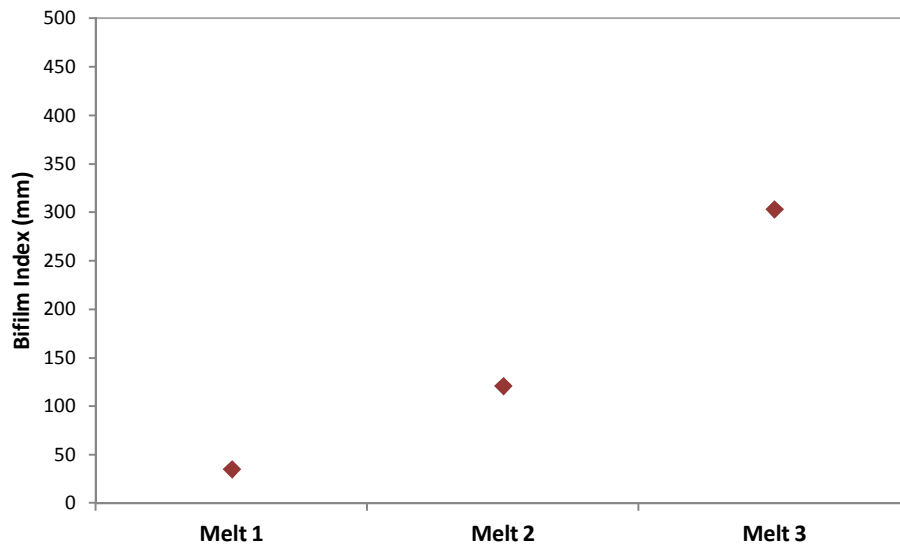

Figure 4-5 Average bifilm index of each melt

With regard to the relation between porosity percentage and density from density measurement experiment; it is important to note that there is a clear relationship between density and bifilm index. Accordingly, the samples from the third melt with highest bifilm index have the lowest density and so on. Figure 4-6 shows this relationship between bifilm index and density.
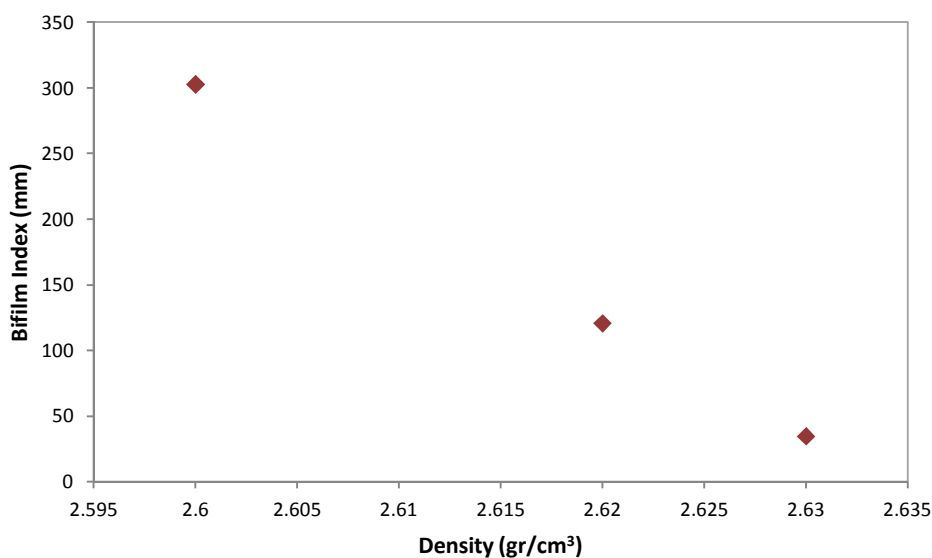

Figure 4-6 Comparison of average amount of bifilm index and density of each melt

4.3 PoDFA Analysis

Three PoDFA samples were sectioned and prepared for metallographic examination. Samples were examined using an optical microscope to identify and count the inclusions.

All the samples contained trace levels of MgO, Mg-cuboids, spinel and carbides, and all had a small number of fine oxide films. Micrographs of each sample prove the presence of these inclusions. Results of the quantitative analysis are reported in Table 4-3 and presented as a bar chart in figure 4-7.

Table 4-3 Summary of inclusions from each melt

|	Melt No.		1	2	3
	inclusion	Chemical	Unit		
Oxide Films	**Number**	$\gamma\text{-}Al_2O_3$	[#/kg]	**17**		**4**
	length			**Mixed**		**Mixed**
	thickness			**Mixed**		**Fine**
Carbides	Small Carbides	$Al_4C_3 < 3\mu m$	mm^2/kg %	Trace	Trace	Trace
	Large Carbides	$Al_4C_3 > 3\mu m$	mm^2/kg %	Trace	Trace	Trace
Magnesium Oxides	Magnesium Oxide	MgO	mm^2/kg %	Trace	Trace	Trace
	Cuboid	$MgAl_2O_4$- Cuboid	mm^2/kg %	Trace	Trace	Trace
	Metallurgical Spinel	$MgAl_2O_4$-Spinel	mm^2/kg %	Trace	Trace	Trace
Refractory Materials	Reacted refractory	Spinel-like	mm^2/kg %			
	Unreacted Refractory	$\alpha\text{-}Al_2O_3$, CaO, SiO_2,...	mm^2/kg %	0.332 99%	Trace	Trace
		C (graphite)	mm^2/kg %			
Additions	Boron Treatment	(Ti, V)B_2	mm^2/kg %			
	Al-Oxide	Al_2O_3	mm^2/kg %	Trace	Trace	0.24 99%
	Grain Refiner	TiB_2/TiC	mm^2/kg %			
Total Inclusion Content				0.332		0.24
Total without Grain Refiner				0.332		0.24
Comments				Unidentified refractory particles	Sample ran through, incomplete inclusion band	Clustered Al_2O_3
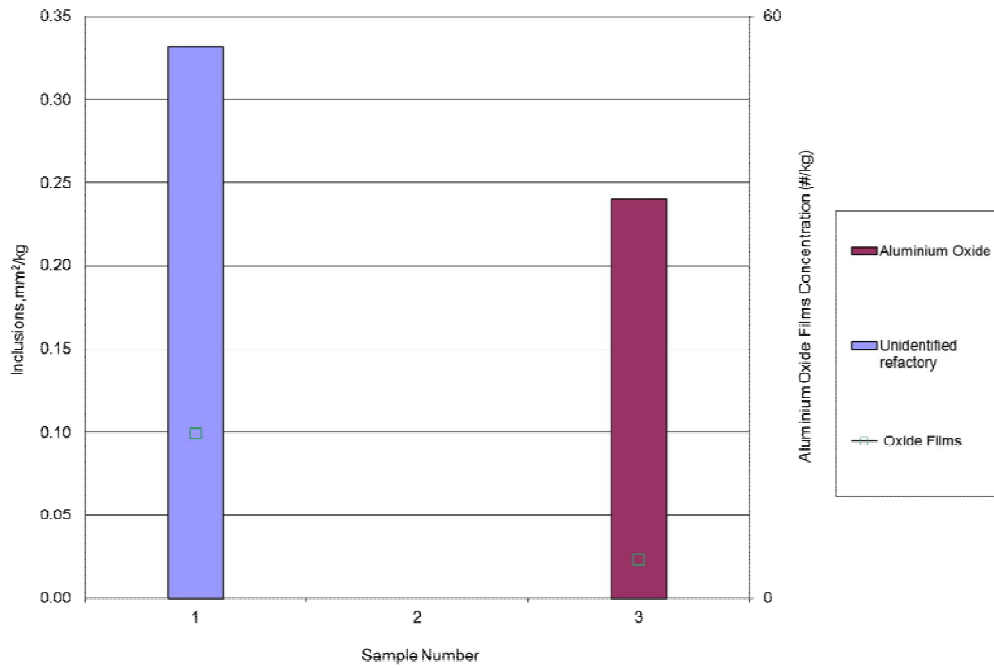
Figure 4-7 Results of PoDFA experiment

The Brief description about the inclusion presents in each of the melt is given with micrographs evidence:

Melt 1: This sample contained a large number of angular particles, as shown in Figure 4-8; the inclusions appear to be a refractory material.
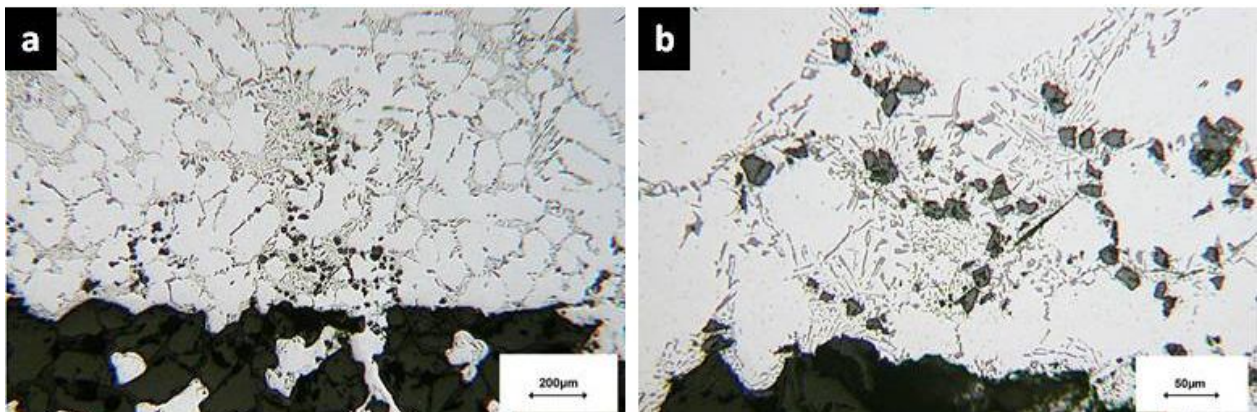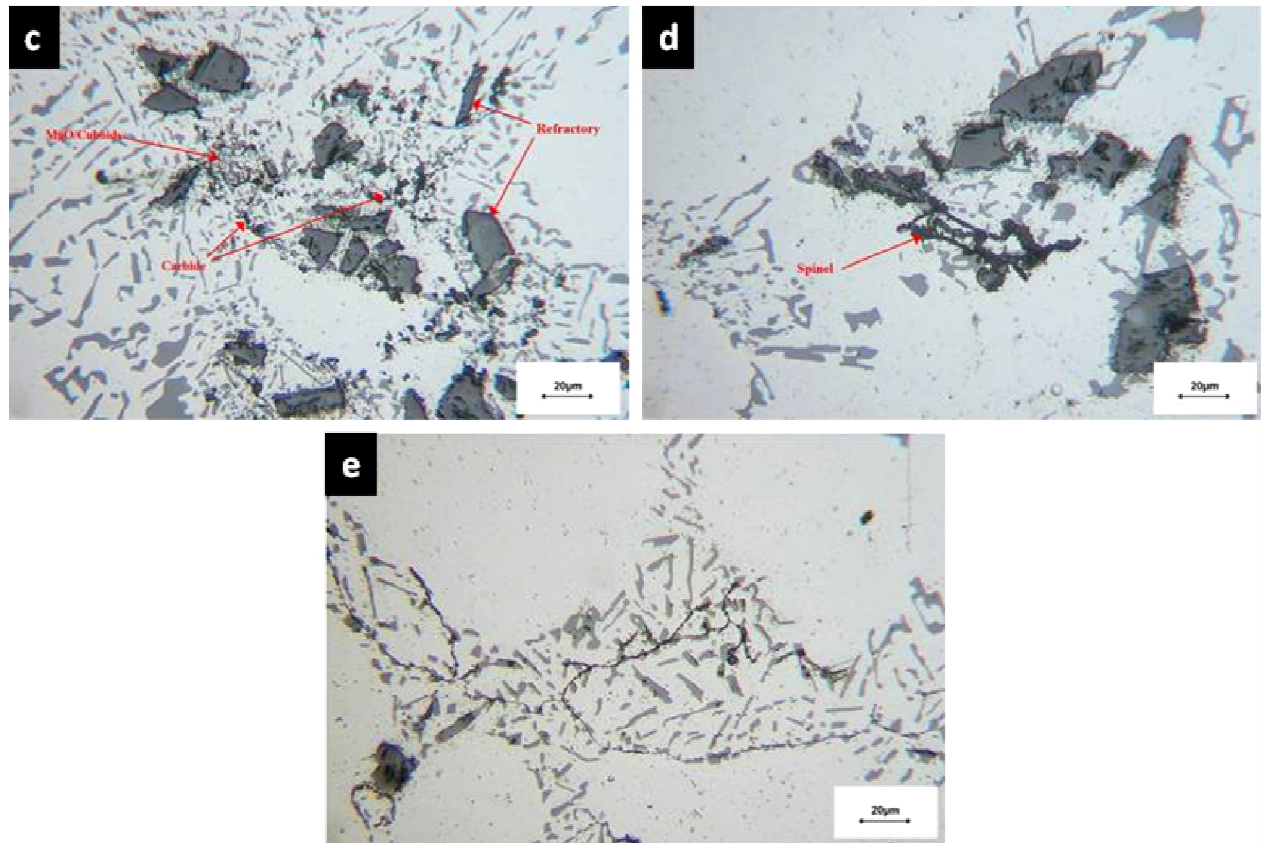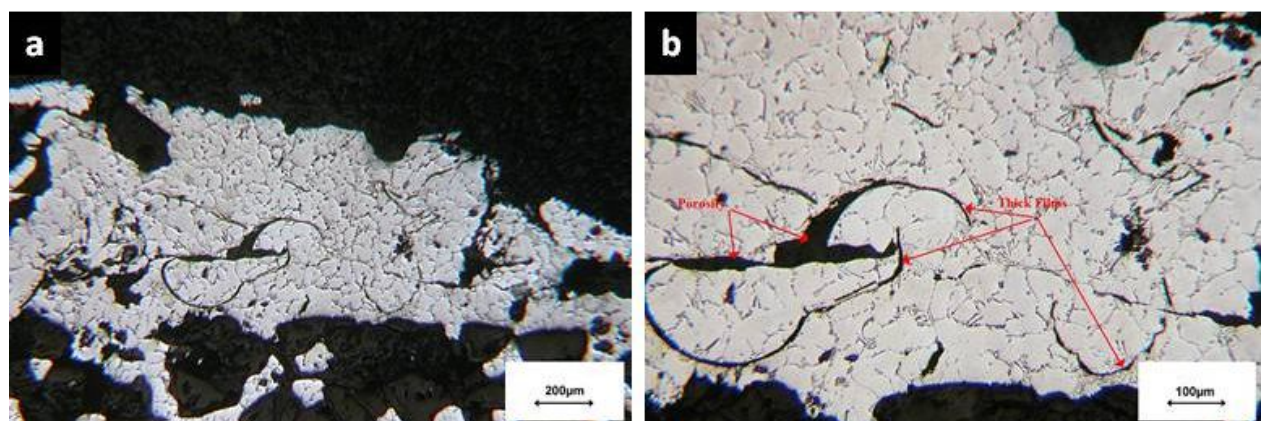
Figure 4-8 Photomicrographs of PoDFA samples from melt 1: a) general view; b) refractory inclusions; c) inclusions; d) spinel; e) thin oxide film

Melt 2: This sample contained several thick oxide films that had reacted with the melt and were converting to spinel, as shown in Figure 4-9. The metal had completely run through the filter during the PoDFA test leaving a thin and incomplete solid residue on the filter surface. A quantitative assessment could not be carried out.
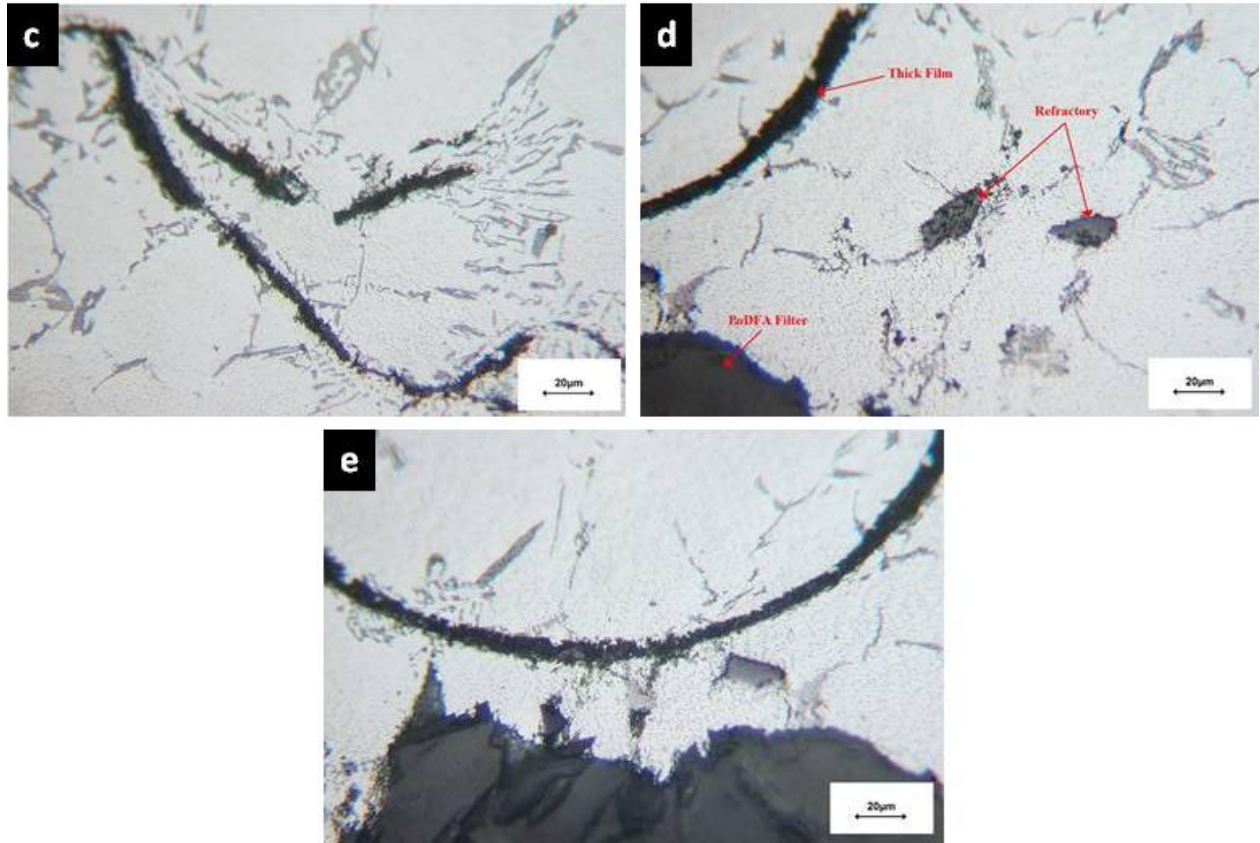
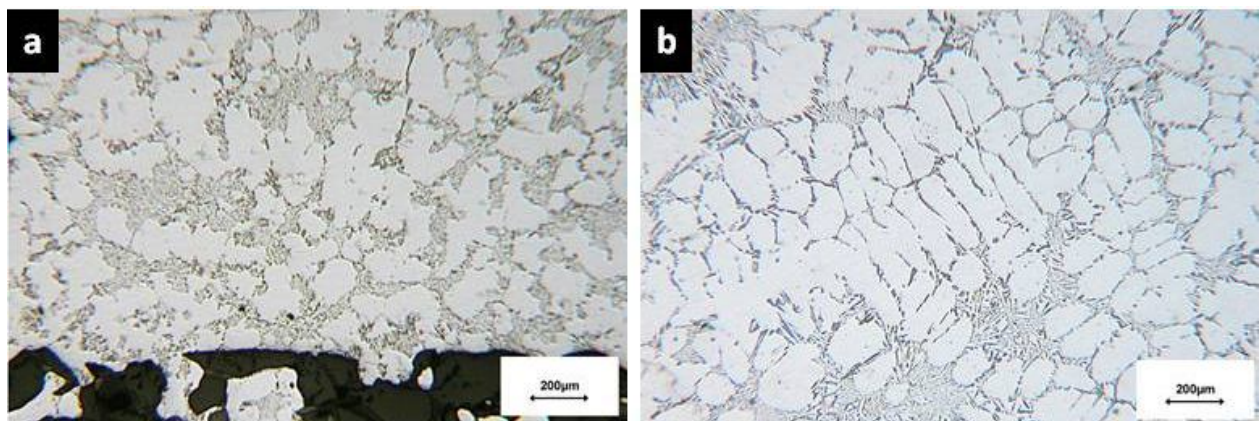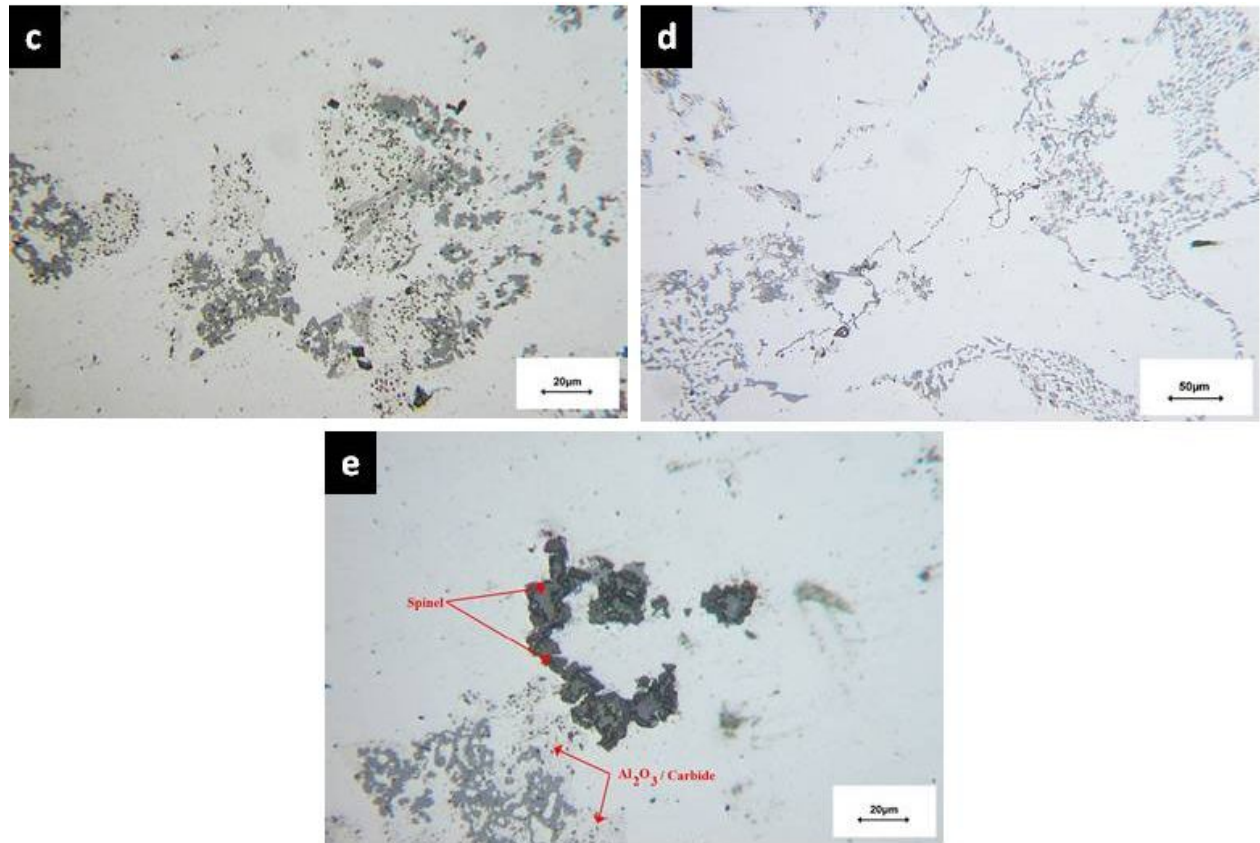*Figure 4-9 Photomicrographs of PoDFA samples from melt 2: a) general view; b,c,e) thick films; d) inclusions*

Melt 3: Clusters of a fine particulate dominated the inclusion band, as shown in Figure 4-10. It is concluded that these are Al_2O_3 particles from the rod addition. The eutectic microstructure was noticeably different in the inclusion band compared with the metal outside of the band.

Figure 4-10 Photomicrographs of PoDFA samples from melt 3: a) general view; b) microstructure outside inclusion band; c) Al₂O₃ clusters; d) thin oxide film; e) inclusions

It is usual to observe trace levels of MgO, Mg-cuboid and spinel inclusions in alloys containing magnesium. It is also normal to see carbides, particularly in melts made from primary aluminium as a result of reaction with the carbon anode in the electrolytic cell.

The particles in Sample 1 have the appearance of a refractory material. They are similar in appearance to the material of the PoDFA filter, suggesting they may be silicon carbide.

The thick films in Sample 2 are typical of melts made from anodized scrap. In alloys containing magnesium it is normal for the films to react with the melt to form thick spinel films.

The clustered particles observed in Sample 3 are assumed to be Al_2O_3 particles from the rod addition. The particles appear to have promoted a change in the morphology of the eutectic silicon.

4.4 Bending test

The bending specimen was examined until a complete crack appears on the surface and the maximum force has been registered. Figure 4-12 and 4-13 present the average force and bend strength of all three melts. The results from bending tests will be discussed as well. Figure 4-11 compared three samples to illustrate their difference.
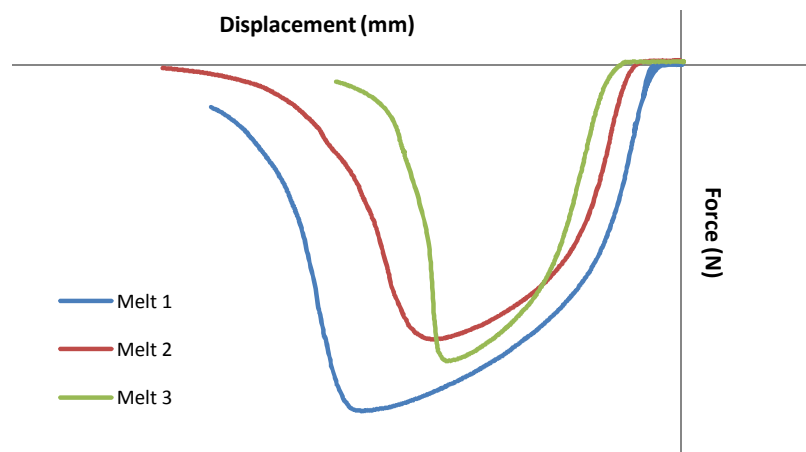

Figure 4-11 Comparison of three random samples from each three melts
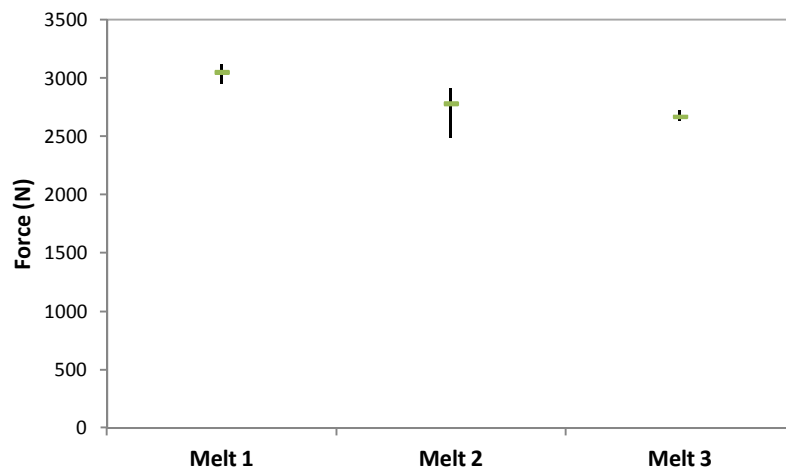

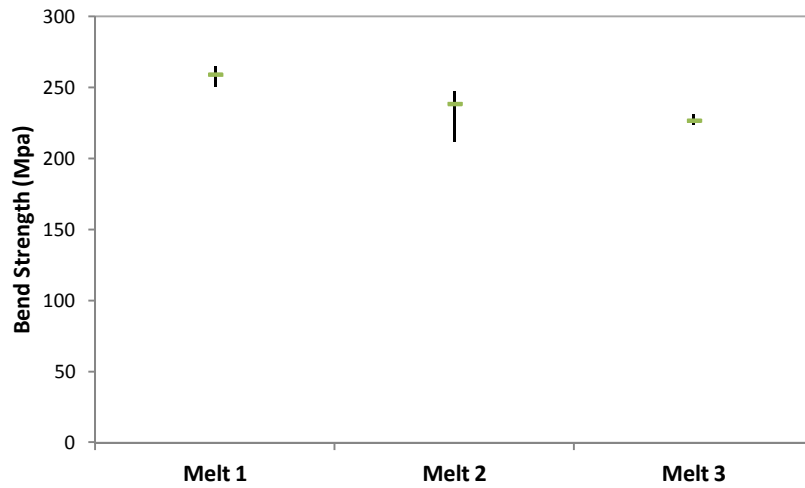*Figure 4-12 The comparison of average force for each melt*

Figure 4-13 Bend Strength of each melt

Figure 4-14 established a correlation between bend strength and bifilm index. This was expected that bend strength will decrease when bifilm index increases.
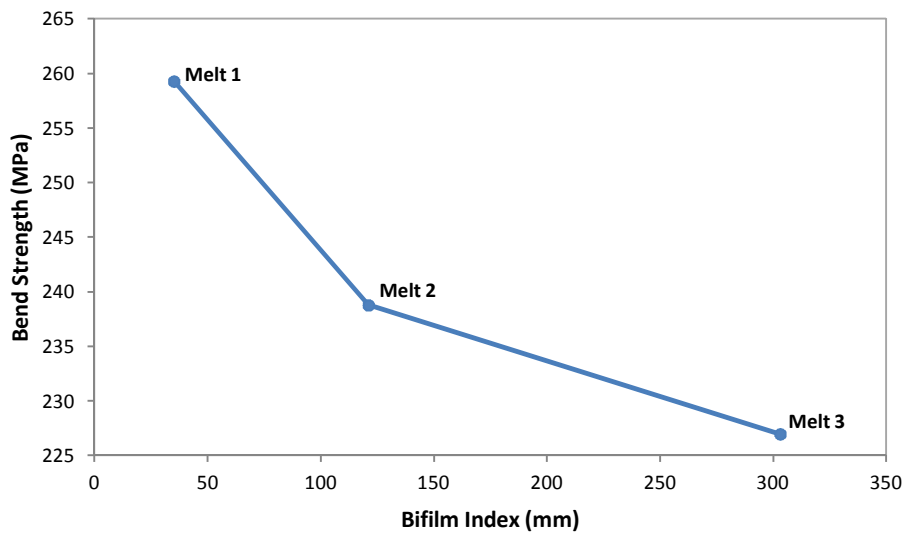
Figure 4-14 Bend strength changes with different bifilm index

61

4.5 Tensile Test

The results of the tensile tests for fracture strength, yield strength, and fracture elongation are categorized and the value of each melt is a mean value composed of 20 samples.

4.5.1 Yield Strength

Yield stress is defined as the end of the elastic regime, the onset of irreversible plastic deformation, $\sigma_{0.2}$, which is the stress where the remaining strain would be 0.2%. Following figures show the results of yield strength of each melt.
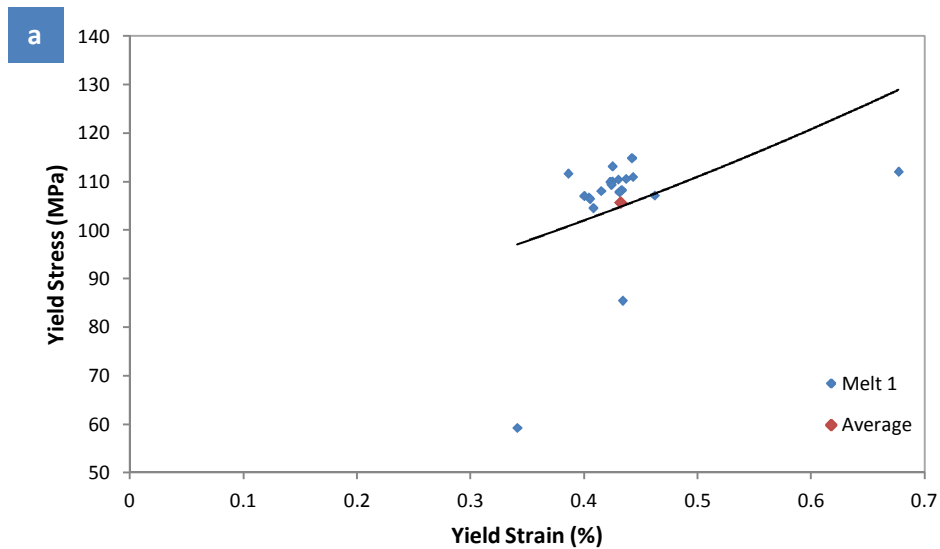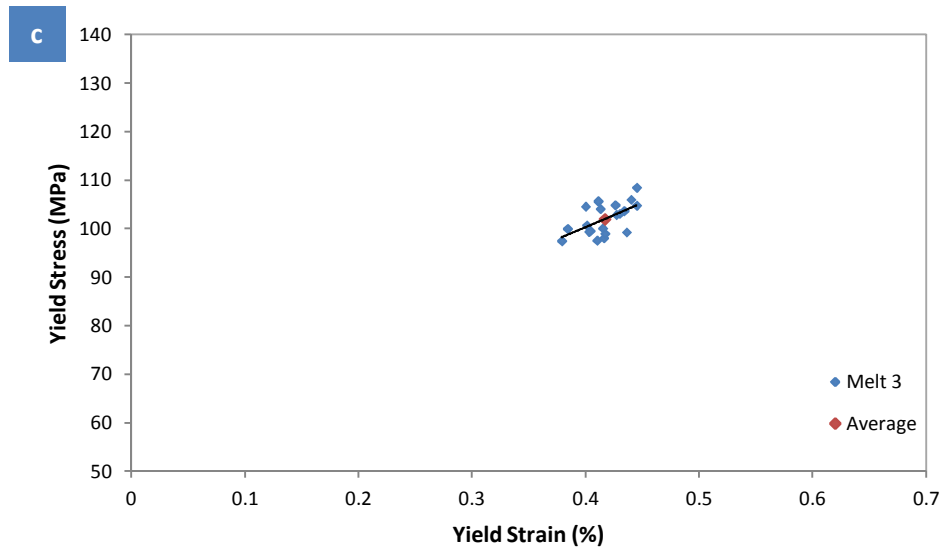
Figure 4-15 Yiels stress-strain diagram: a) melt 1; b) melt 2; c) melt 3
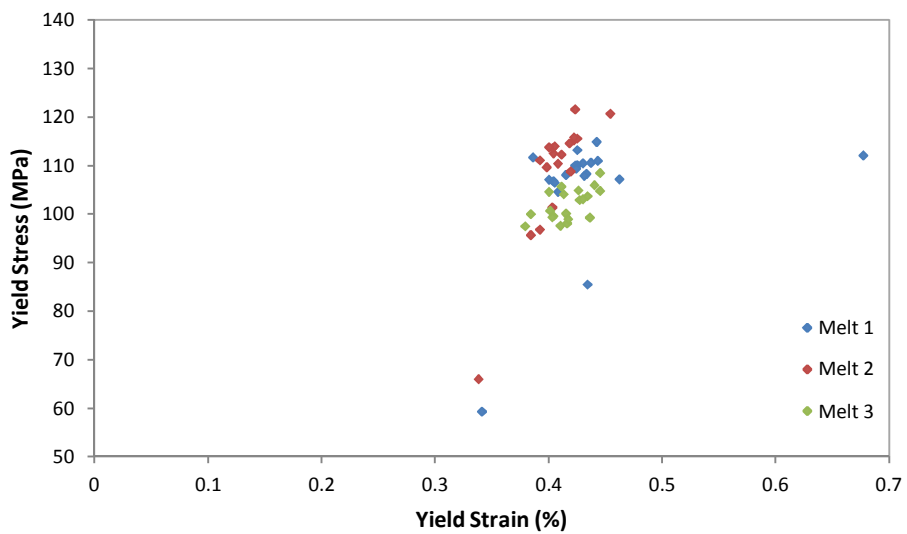
Figure 4-16 Yeild stress-strain diagram

4.5.2 Ultimate Tensile Strength (UTS)

The strength of a material is its ability to withstand external forces without breaking. Two parameters are defined regarding strength of material. Fracture strength is the load at fracture divided by the final cross-sectional area; and ultimate tensile strength (UTS) is defined as the maximum load divided by the initial cross-sectional area [42]. As most of samples were

broke near to ultimate tensile strength, then it is reasonable to assume that both parameters equal. Figure 4-17 present ultimate tensile strength UTS of each samples.
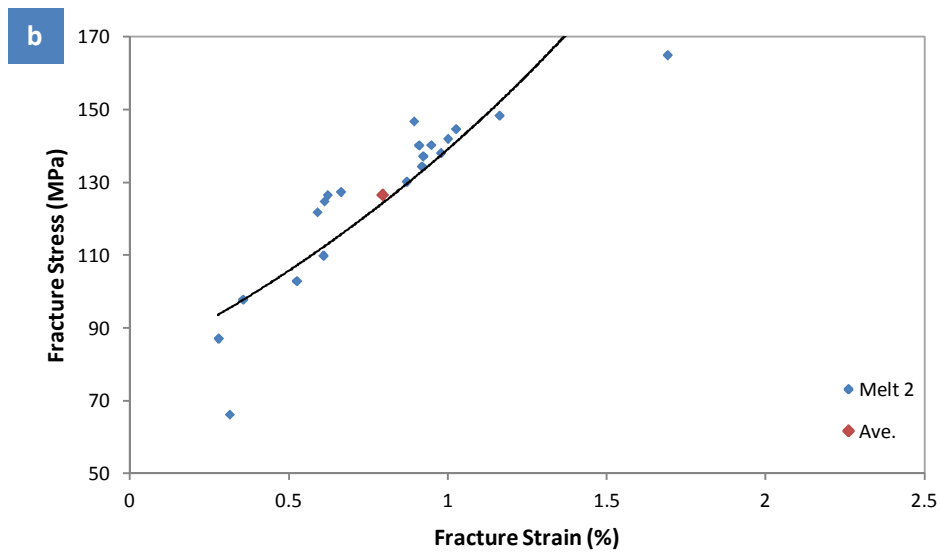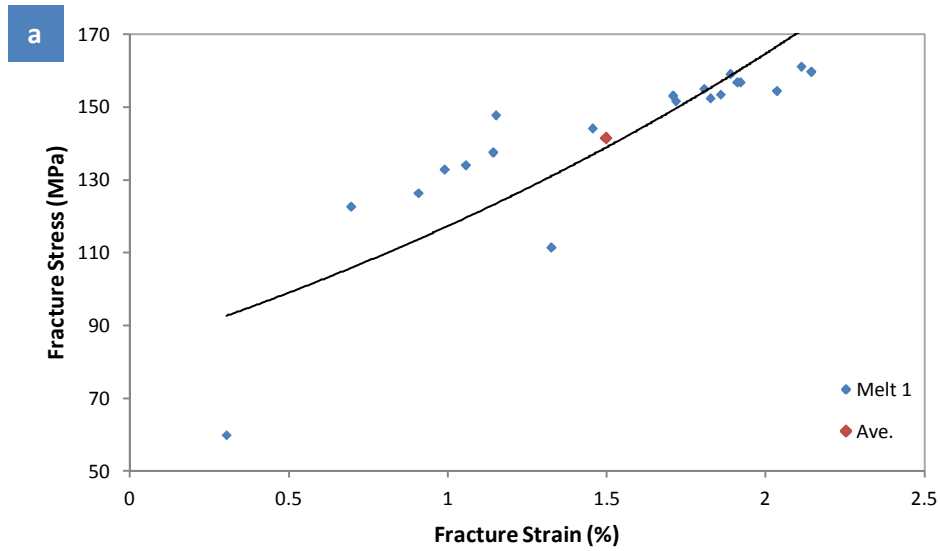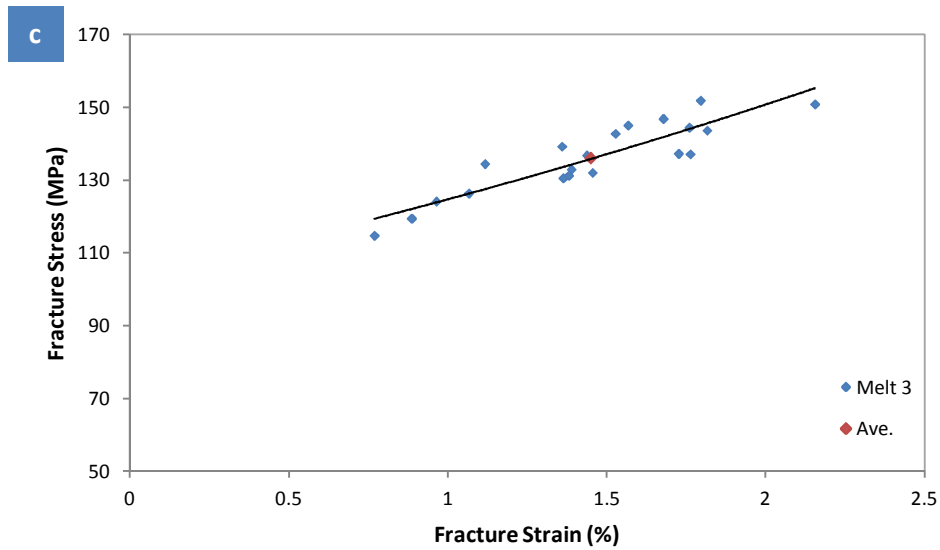
Figure 4-17 Ultimate tensile strength (UTS)-strain diagram: a) melt 1; b) melt 2; c) melt 3
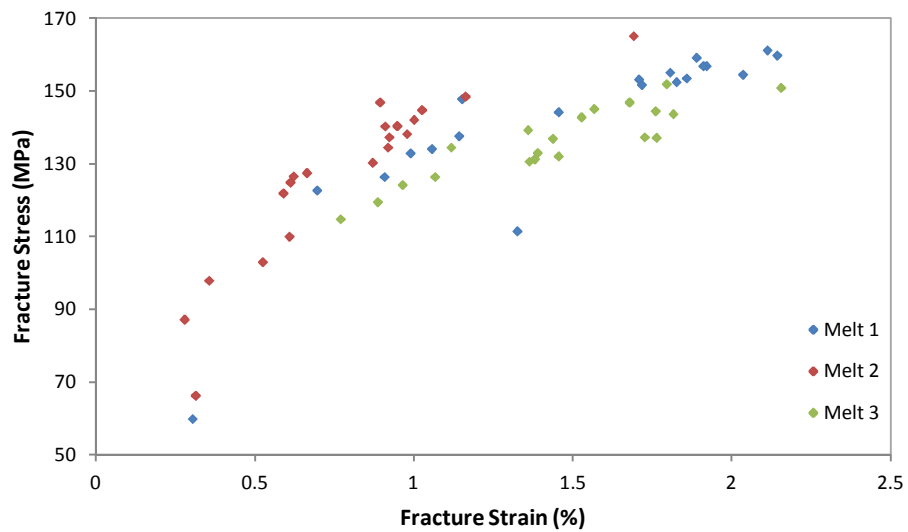
Figure 4-18 Ultimate tensile strength (UTS)-strain diagram

4.5.3 Elongation

The percentage elongation is reported as the maximum elongation of the gage length divided by the original gage length, or the reduction of area. The elongation percentage is referred to ductility and it indicates the ability of a material to deform easily under tensile

force; or withstand plastic deformation without rupture. Figure 4-19 shows the elongation percentage of different melts.
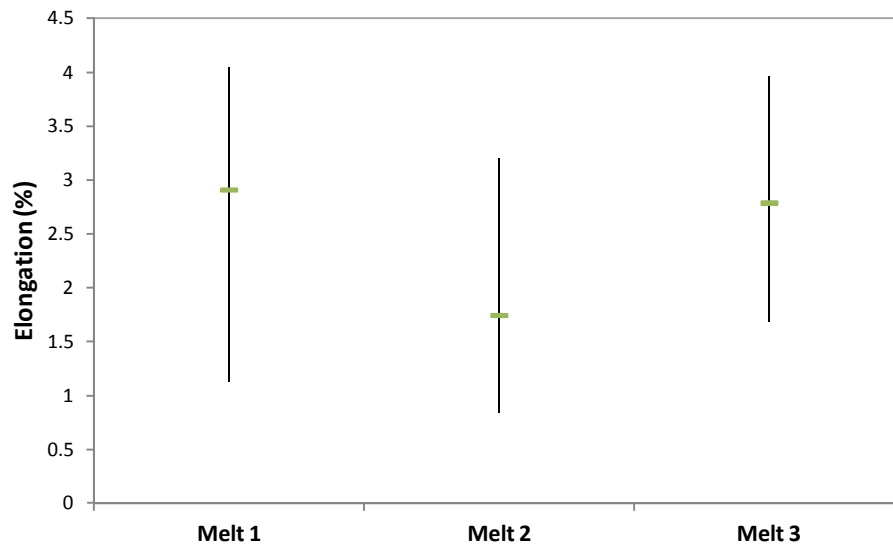
Figure 4-19 Comparison of elongation

The most important aspect of study was to investigate the relationship between bifilm index and mechanical properties. Accordingly, it was expected that bifilm index could determine the decreasing trend from melt 1 to melt 3, respectively. But melt 2 surprisingly showed the highest yield strength while had the lowest ultimate tensile strength, as shown in figures 4-20 and 4-21. To discover the main reason, one is to compare the stress and strain trend of each melt, figure 4-23 and 4-24.
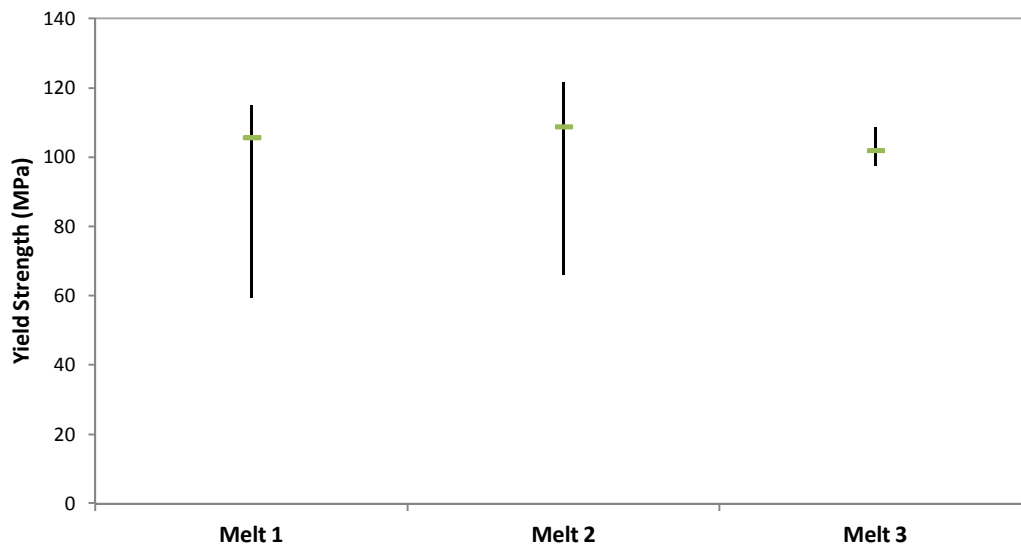
Figure 4-20 Comparison of average yield strength of each melt
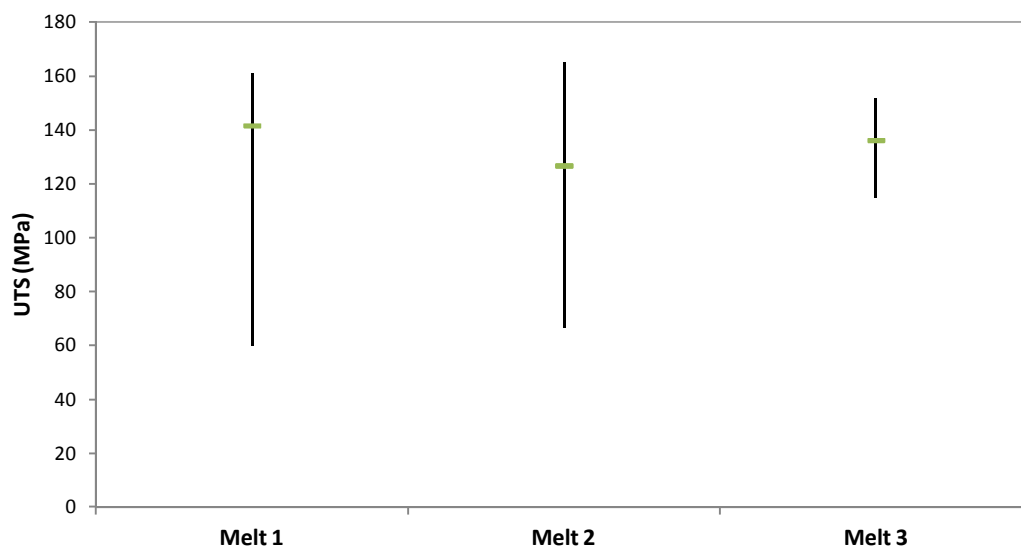
Figure 4-21 Comparison of average UTS of each melt

According to figure 4-23, however melt 2 showed the highest yield strength, but it happened at the lowest strain. Furthermore, melt 2 had lowest ultimate tensile strength (UTS) and strain. Therefore, it had the lowest ductility and the most brittle fracture. Figure 4-22 proves this finding since the second group of samples indicated the lowest elongation and tensile strength. None of samples showed necking area or reduction of fracture surface. Moreover, brittle materials have a fracture strain below 0.1% [44] and the average fracture

strain of samples from second melt is 0.8% and accordingly, melt 2 revealed a brittle behavior, rather than ductile.
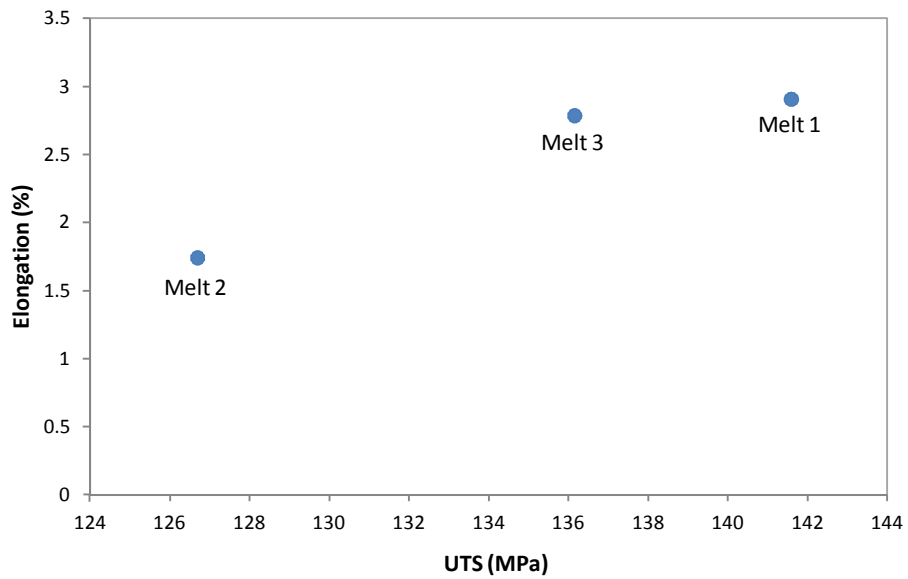
Figure 4-22 Comparison of average UTS and elongation of each melt
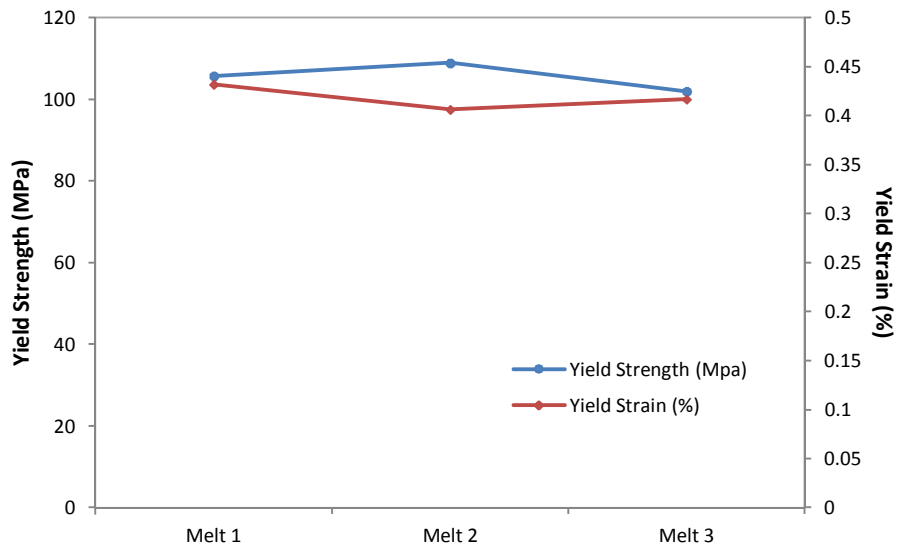
Figure 4-23 Comparison of yield strength and strain of each melt
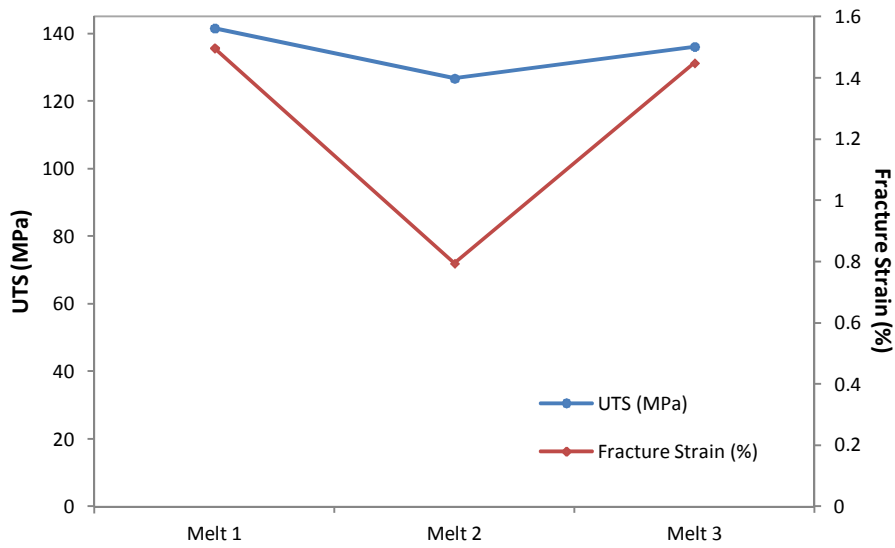
Figure 4-24 Comparison of fracture strength and strain of each melt
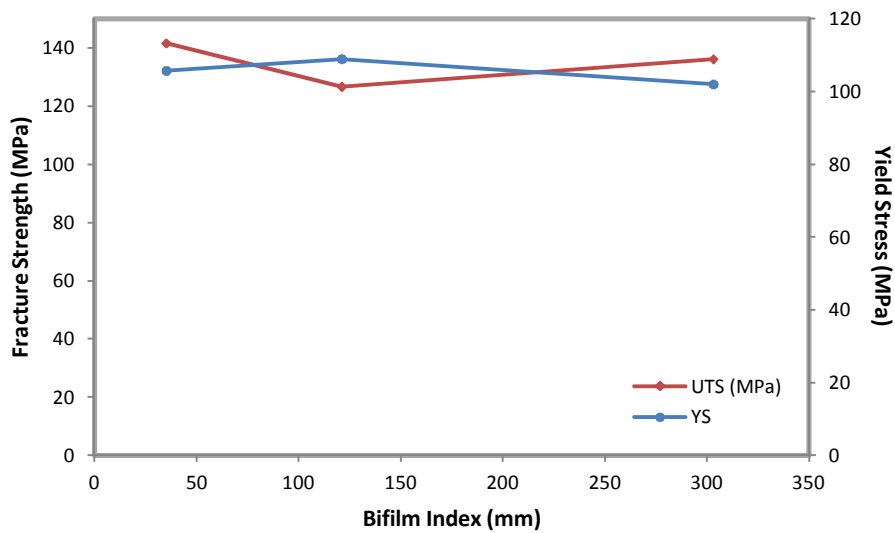
Figure 4-25 Fracture and yield strength change with bifilm index

The most likely explanation for these findings might define by PoDFA results and shape of porosities in melt 2. It is suspected that several thick oxide and spinel layers, plus planar shape of porosities, perpendicular to direction of stress, as a result of addition of anodized plates, might all have contributed to thicker and more open bifilms that would have reduced ductility. The shape of porosities in the RPT samples might help to realize the effect of crack length and radius on failure. Figure 4-26 obviously shows the pores are sharper and planar in melt 2 in comparison with melt 3.
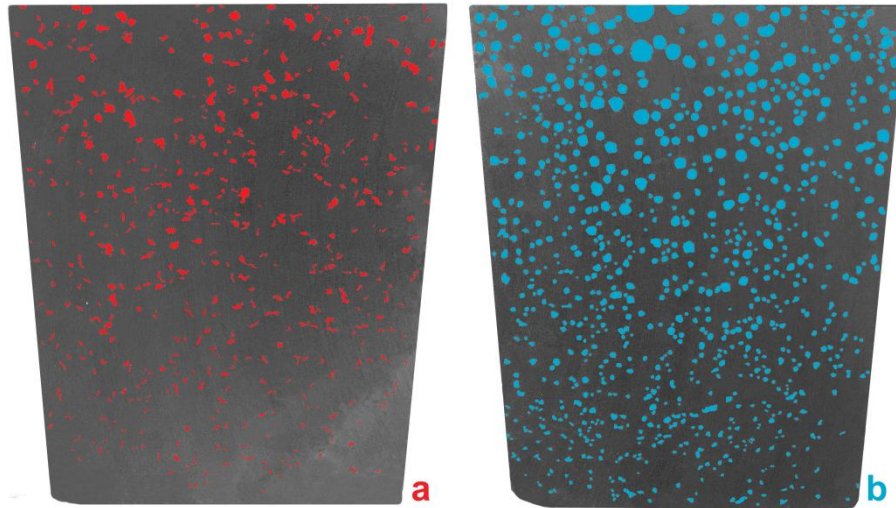
Figure 4-26 Sectioned surfaces of RPT samples: a) Melt 2; b) Melt 3

Most of pores are narrow and planar in melt 2; conversely, melt 3 has the nearly round porosity. It is important to recognize the effect of crack length and radius on stress concentration in samples.

The crack might initiate from a sharp crack edge and grows rapidly along the other cracks with the same geometry. Then melt 2 had the lowest ductility while melt 3 shows a little higher property due to round pores.

4.6 Image Analysis

Ten samples from each melt were chosen and their polished surface has been scanned by a light microscope. The pictures were digitized and analyzed by image analysis *easylab6* software and the results were used to plot a graph of equivalent diameter, roundness, and porosity distribution. Figure 4-27 shows the images of different samples after digitizing and analyzing.
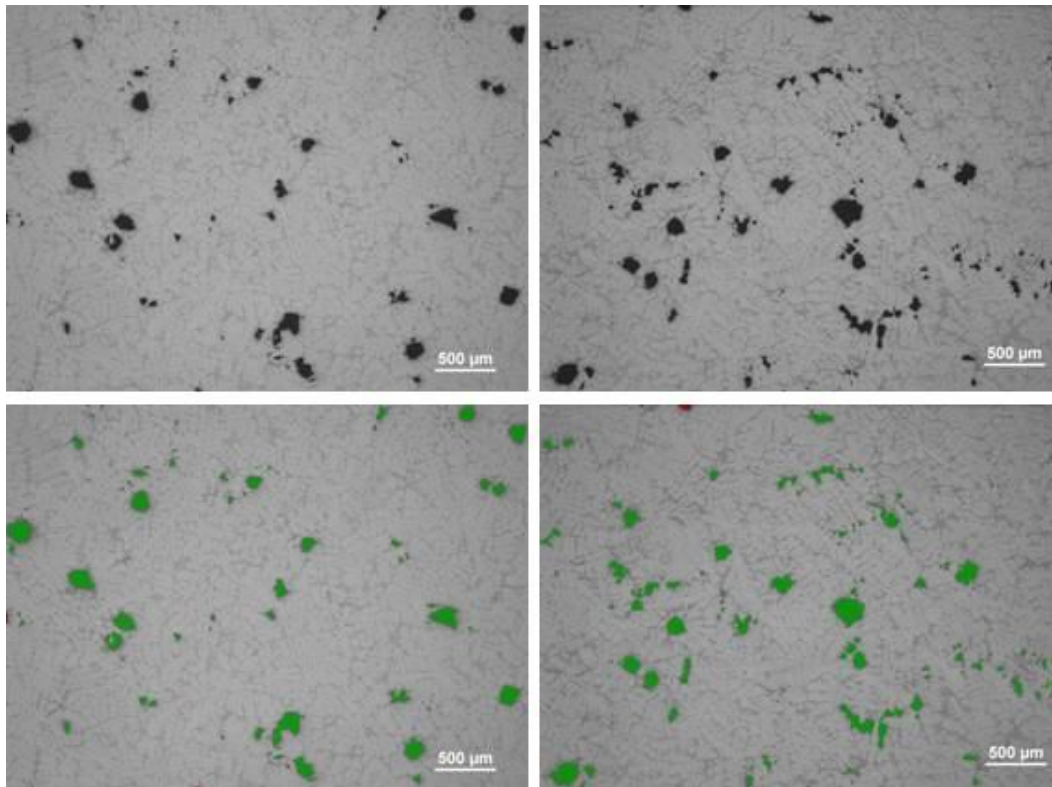
Figure 4-27 Digitized pictures, before and after analyzing; green spots are detected porosities

Figures 4-28 and 29 compare the diameter and roundness of pores in three series of samples and they would help to extend and confirm the theory of failure in tensile test. The pore distribution of each group of samples is showed in figure 4-30.
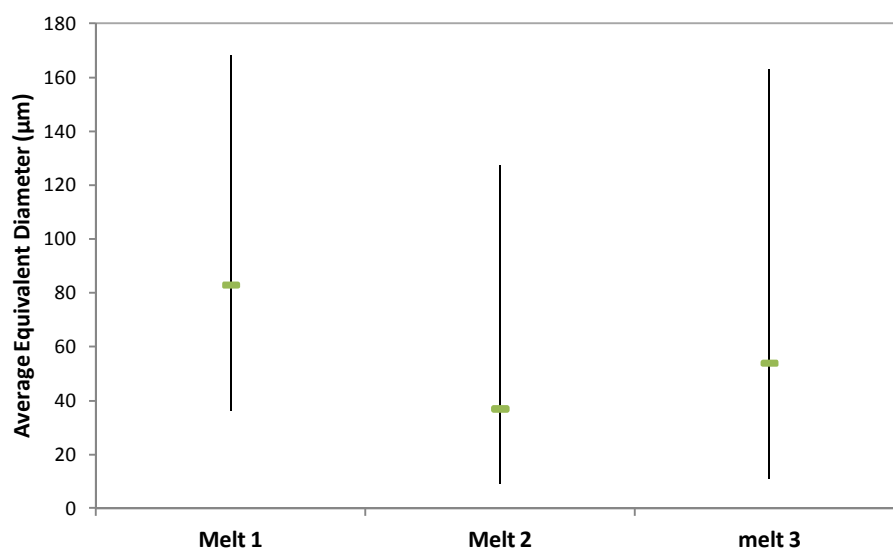
Figure 4-28 Comparison of average porosity diameter of samples from each melt
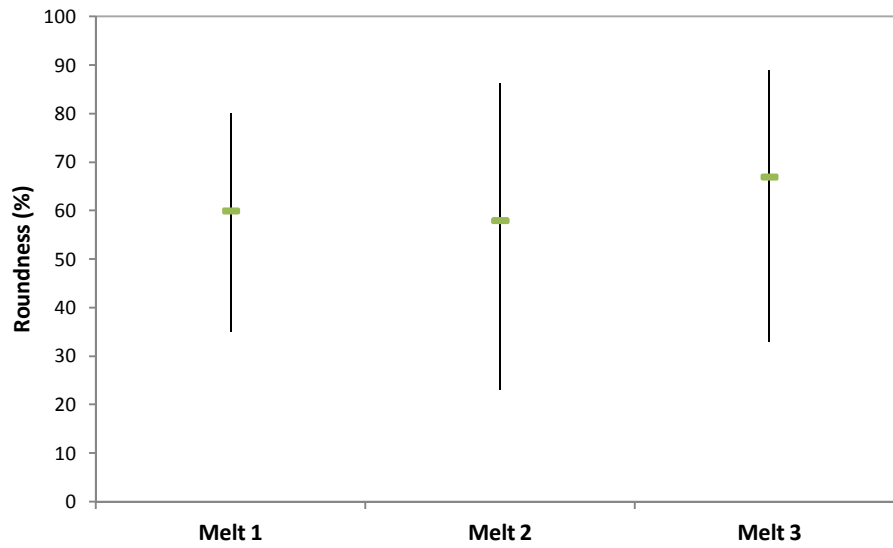
Figure 4-29 Comparison of average roundness of porosities from each melt

According to pore size distribution of samples, second and third melt have small pores with a diameter less than 50 µm. The higher density of small pores in samples from melt 2 and 3, in comparison with melt 1, could be the main reason of lower mechanical properties.
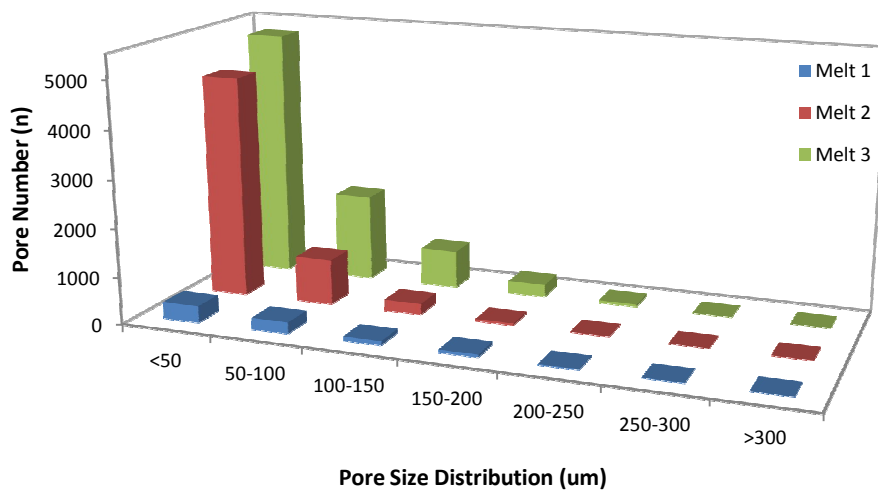
Figure 4-30 Distribution of porosities in each melt

The roundness of pores in second melt samples is lowest and it might cause a higher stress-concentration factor in these samples. Furthermore, high density of pores in a certain area of samples gives rise to a rapid initiation and growth of cracks. The effect of thick oxide and spinel may have a strong influence on mechanical properties.

4.7 Scanning Electron Microscope (SEM)

From each series of samples, the samples with highest and lowest fracture strength were chose to investigate their fracture surface by scanning electron microscope (SEM). The dendrites, oxide and spinel layers, and porosities can be seen in following pictures and they can illustrate how dendrites in the pores are covered by oxide. SEM analysis of the fracture surfaces confirmed the presence of oxide films on the dendrites surface inside pores.
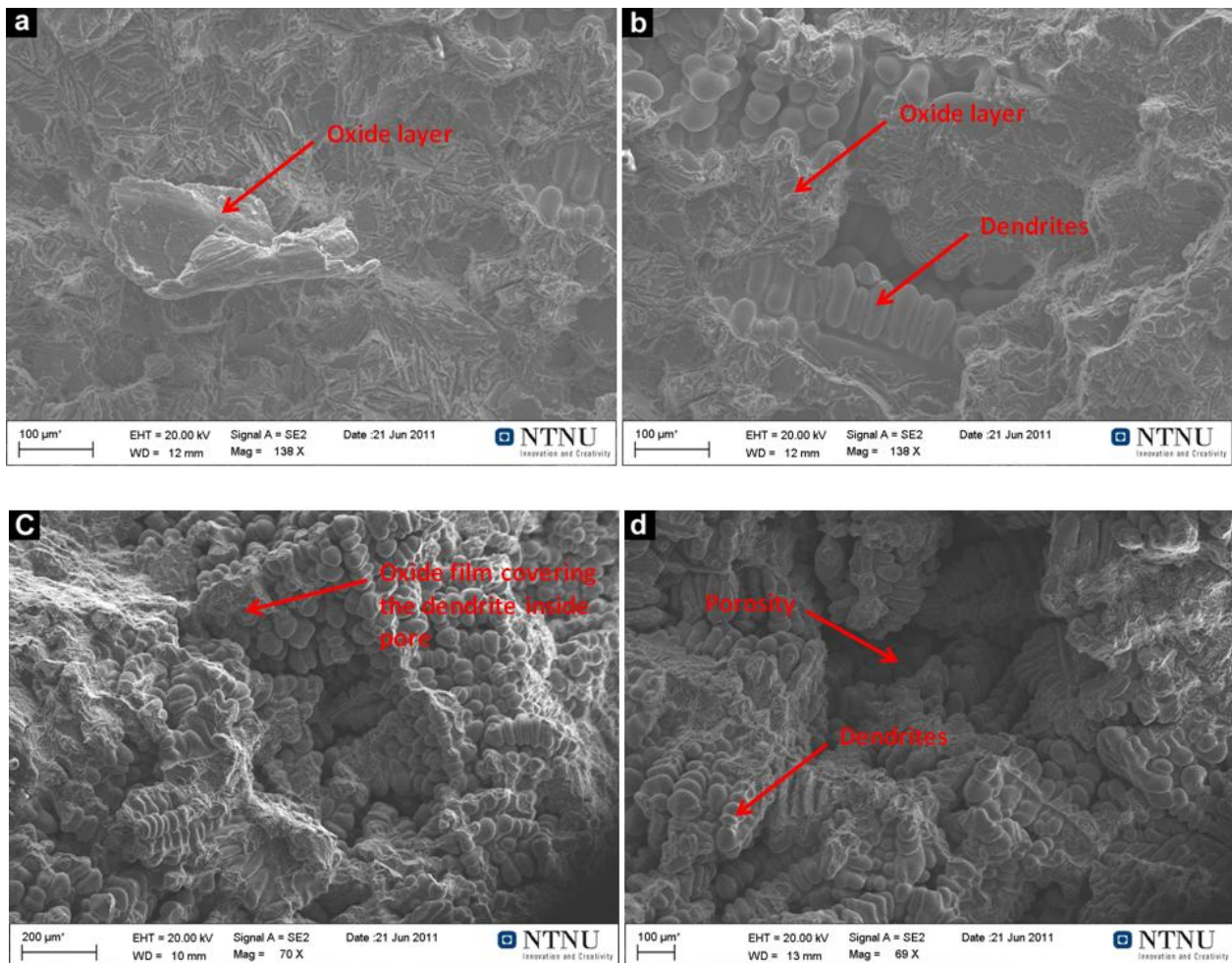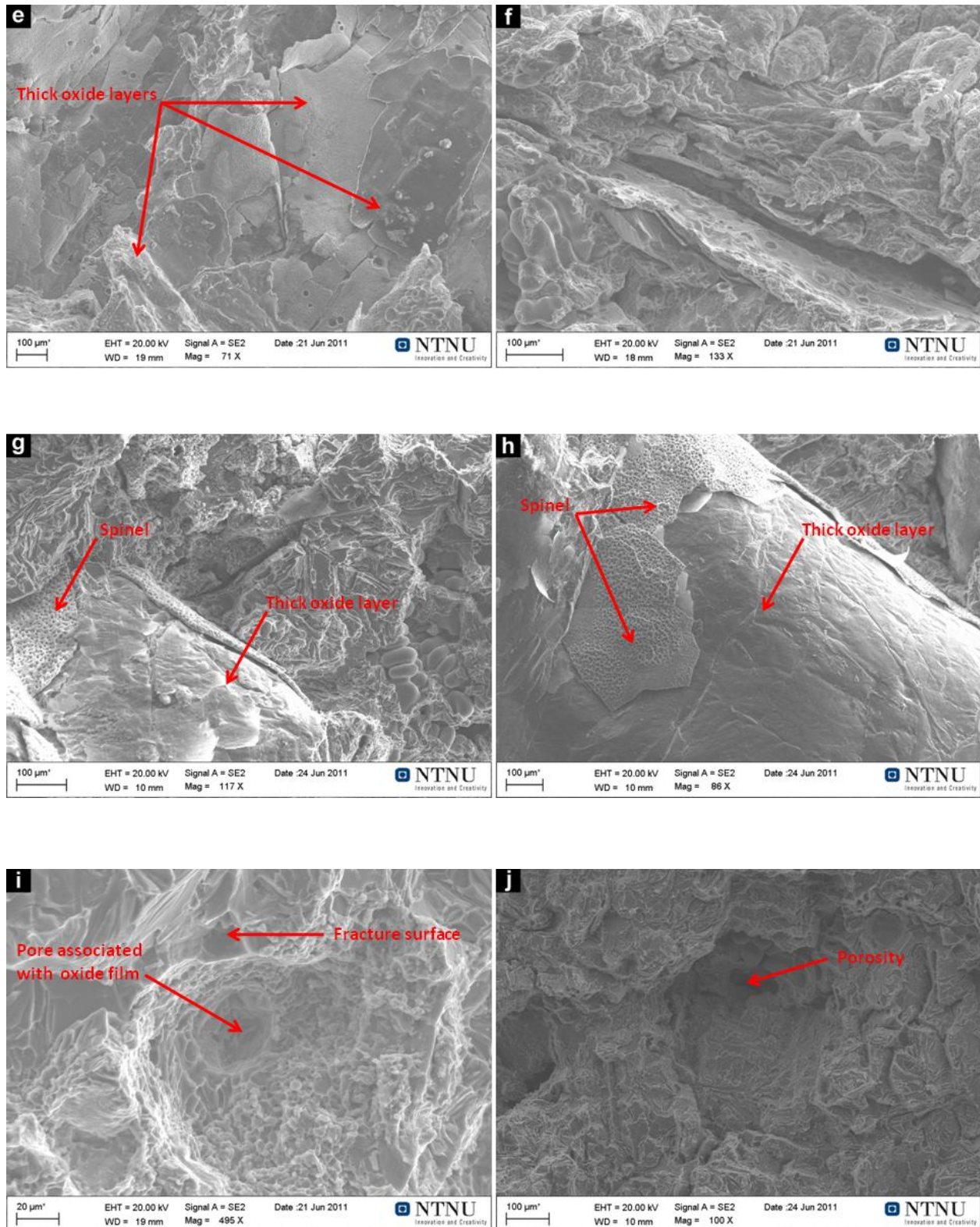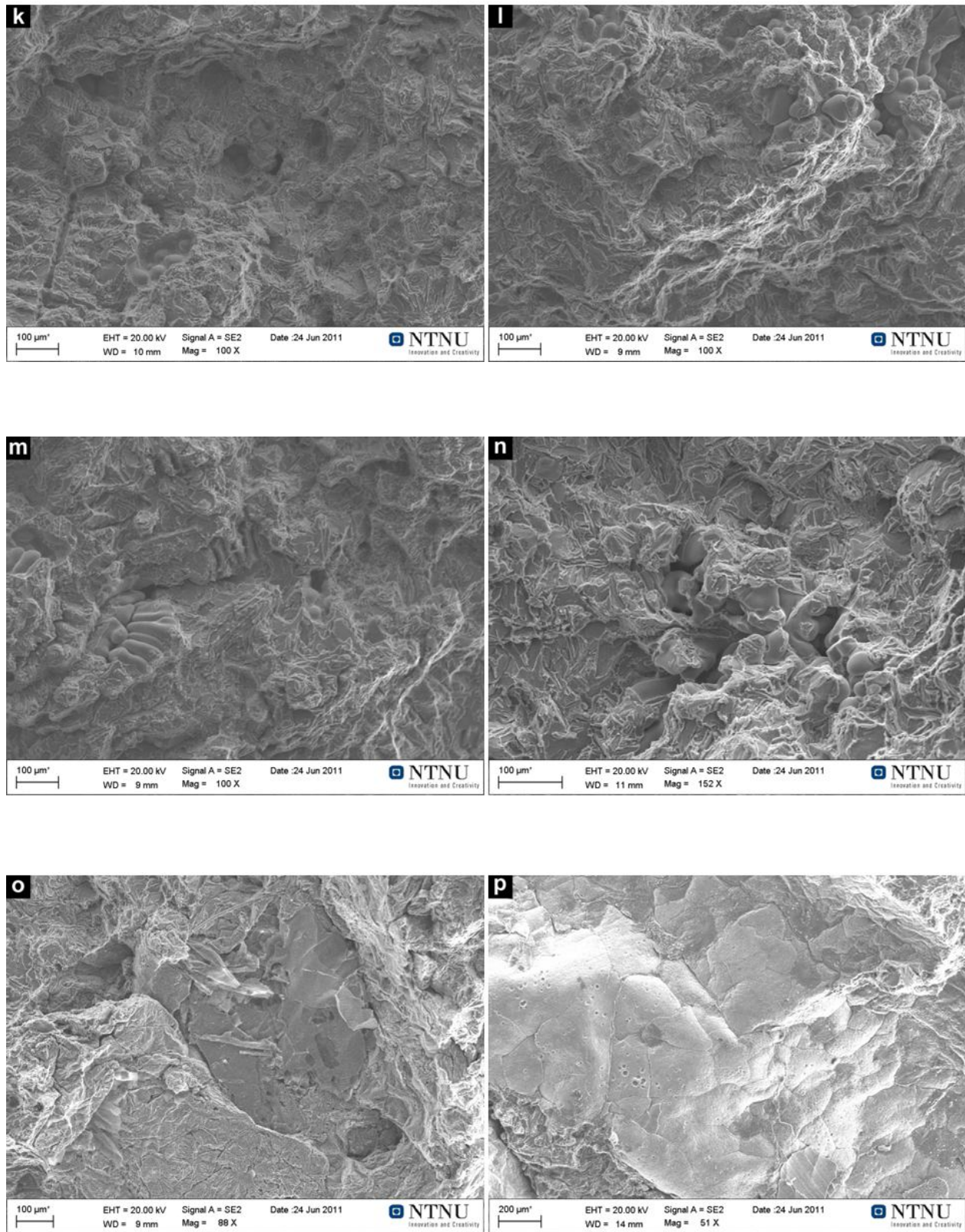
Figure 0-1 SEM pictures from fracture surface of bending samples: a,b,c,d) melt 1; e,f,g,h) melt 2; i,j,k,l,m,n,o,p) melt 3

5 Conclusion

The main objective of this work is to examine the influence of different levels of entrained oxides on the mechanical properties of the A356 alloy under constant hydrogen concentration. Based on the experimental results the following conclusions were drawn:

- The volume percentage porosity is almost the same in all casting samples under constant hydrogen conditions.

- The bifilm index, the total length of bifilms on the sectioned surface of the RPT sample, established a proper evaluation of the melt quality and the amount of bifilms. Bifilm index data from RPT shows that oxide addition has significant impact on melt quality degradation.

- PoDFA test confirms the presence of thick oxide films and spinel in all samples.

- Pore size distribution indicates that third melt with high number of oxide-nuclei have significantly higher number of small pores in comparison with other melts.

- The results derived from bending test showed the higher amount of bifilms result in reduction of bend strength.

- The results derived from tensile tests showed shape and distribution had additional effect on tensile properties. Moreover, it should be noted that thick oxide layer and spinel had a major influence on lowering the tensile properties of second group of samples.

- SEM observation of fracture surfaces showed pores are associated with oxide films.

6 Recommendation for Future Work

Although progress has been made in this thesis towards understanding the effects of bifilms in constant hydrogen content, it is recommended to perform more tensile tests with different alloys and casting conditions to investigate the correlation between bifilm index with mechanical properties. A valuable target of these trials would be to study the effect of thickness, shape, and distribution of bifilms on mechanical properties of casting alloys.

It is also necessary to study the interactions between bifilm and other defects, such as Fe-rich phases. The presence of other oxides and spinel such as magnesium oxide, silicon oxide, $Al_2O_3.MgO$ and their effect on mechanical properties could be the subject of further investigations.

7 References

1. **Dispinar, D. and Campbell, J.** *Use of bifilm index as an assessment of liquid metal quality.* Birmingham : s.n., 2006, International journal of cast metals research, Vol. 19.

2. **Dispinar, D. and Campbell, J.** *Critical Assessment of the Reduced Pressure Test; Part 2: Quantification.* July 2004, International Journal of Cast Metals Research, Vol. 17.

3. **Samuel, A. M. and Samuel, F. H.** *Porosity Factor in Quality Aluminium Castings.* Chicoutimi : s.n., AFS Transactions.

4. **Patterson, W. C.** *Technological Trends in the Automobile Industry and Their Impact on Aluminium Usage.* 1980, Technological Forecasting and Social Change, pp. 205-216.

5. *www.eaa.net.* [Online] European Aluminium Association. [Cited: July 18, 2011.] http://www.eaa.net/.

6. **Akhtar, Sh.** *Hydrogen Porosity in Al-Si Foundry Alloys.* Department of Materials Science and Engineering, Norwegian University of Science and Technology. Trondheim : s.n., 2010. PhD Thesis. 978-82-471-1946-4.

7. **Campbell, J.** *Castings.* Second. Oxford : Butterworth Heinemann, 2003. 0-7506-4790-6.

8. **Engh, T. A.** *Principles of Metal refining.* s.l. : Oxford University Press Inc., 1992. 0-19-856337-X.

9. **Makarov, S. Ludwig, R. and Apelian, D.** *Electromagnetic Visualization Technique for Non-metallic Inclusion in a Melt.* USA : s.n., 1999, Materials Science Technology, Vol. 10, pp. 1047-1053.

10. **Dispinar, D.** *Determination of Metal Quality of Aluminium and Its Alloys.* School of Metallurgy and Materials, The University of Birmingham. Birmingham : s.n., 2005. PhD Thesis.

11. **Seniw, M. E., Conley, J. G. and Fine, M. E.** *The effect of Microscopic Inclusion Locations and Silicon sefregation on Fatigue Lifetimes of Aluminium A356 Castings.* s.l. : Elsevier, 2000, Materials Science and Engineering, pp. 43-48.

12. **Mclaughlin, M., Kim, C. -W. and Kubo, K.** *An Application of Porosity Simulation to an Aluminium Automotive Suspension Component.* s.l. : American Foundry Society, 2002, AFS Transactions, pp. 223-236.

13. **Kaufman, J. G. and Rooy, E. L.** The Influence and Control of Porosity and Inclusions in Aluminium Castings. *Aluminum Alloy Castings: Properties, Processes, and Applications.* s.l. : ASM International, December 2004, p. 340.

14. **Dispinar, D. and Campbell, J.** *Critical Assessment of Reduced Pressure Test; Part 1: Porosity Phenomena.* July 2004, International journal of Cast Metals Research, Vol. 17.

15. **Carlson, K. D., Lin, Zh. and Beckermann, C.** *Modelling of Porosity Formation in Aluminium Alloys.* s.l. : TMS (The Minerals, Metals and Materials Society), 2006.

16. **Pequet, Ch., Gremaud, M. and Rappaz, M.** *Modeling of Microporosity, Macroporosity, and PipeShrinkage Formation during the Solidification of Alloys.* July 2002, Metallurgical and Materials Transactions, Vol. 33A.

17. **Lucas, L. D.** *in Physiochemical Measurement in Metals Research. Techniques of Metals Research.* [ed.] R. Rappaz. New York : s.n., 1970, Interscience, Vol. 4, pp. 219-292.

18. **Nordmark, A.** *Influence of Gas Fluxing with Argon-Hydrogen Mixture and Grain Refinement, on Feeding Behaviour of AlSi7Mg in Gravity Sand Casting.*

19. **Chen, X. -G. and Engler, S.** *Formation of Gas Porosity in Aluminium Alloys.* Aachen : Aachen University of technology (RWTH Aachen).

20. **Tøndel, P. A.** *Grain Refinement of hypoeutectic Al-Si Foundry Alloys.* NTH. 1994. PhD Thesis.

21. **Apelian, D., Sigworth, G. K. and Whaler, K. R.** 1993, AFS Trans., pp. 297-307.

22. **Mohanty, P. S. and Gruzleski, J. E.** 1995, Acta Metal Mater, pp. 2001-2012.

23. **Mohanty, P. S. and Gruzleski, J. E.** 1996, Acta mater, pp. 3749-3760.

24. **Prasada, A. K., et al.** 2006, Wear., Vol. 261, pp. 133-139.

25. **Ramachandran, T. R., Sharma, P. K. and Balasubramaian, K.** India : s.n., 2008. In Proc of 68th World Foundry Congress.

26. **Liu, L. and Samuel, F. H.** 1997, J of Mat Sci., Vol. 32, pp. 5927-5944.

27. *Quantiative Evaluation of Pore Characteristics in Cast Al Alloys.* **Shivkumar, S., Wang, L. and Lavigne, R.** s.l. : The Minerals, Metals & Materials Society, 1993, Light Metals, pp. 829-838.

28. **Liu, L and Samuel, F. H.** 1997, J of Mat Sci., Vol. 32, pp. 5901-5925.

29. **Shahani, H.** *Effect of Hydrogen on the Shrinkage Porosity of Aluminium Copper and Aluminium Silicon Alloys.* 1985, Scand. J. Metall., Vol. 14, pp. 306-312.

30. **Argo, D. and Gruzleski, J. E.** *Reduction and casting of aluminium.* New York : Pergamon Press, 1988. p. 263.

31. **Fang, Q. T., Anyalbechi, P. H. and Granger, D. A.** *Measurement of Hydrogen Porosity in Unidirectionally Solidified Aluminium Alloys.* 1988, Light Metals, pp. 477-486.

32. **Lu, L. and Dahle, A. K.** *Iron-Rich Intermetallic Phases and Their Role in Casting Defect Formation in Hypoeutectic Al-Si Alloys.* March 2005, Metallurgical and Materials Transactions, Vol. 36A.

33. **Makhlouf, M. M. and Dash, M.** 2001, J of Light Metals, pp. 251-265.

34. **Bangyikhan, K.** *Effects of Oxide film, Fe-rich phase, Porosity and their Interactions on Tensile Properties of Cast Al-Si-Mg Alloys.* School of Metallurgy and Materials, The University of Birmingham. Birmingham : s.n., 2005. PhD Thesis.

35. **Taylor, J. A., Schaffer, G. B. and Stjhon, D. H.** UK : University of Sheffield, 1997. in Proc of 4th Decennial International Conference on Solidification Processing. pp. 238-242.

36. **Stein, D.** *Quantitative Nondestructive Tensile Testing of A356/A357 T61 Aluminium Alloy Castings.* 1980, AFS Trans., Vol. 88, pp. 631-644.

37. **Saigal, A.** *Stress and Strain Distribution in Two-Phase Aluminium-Silicon Alloys.* 1986, AFS Trans., Vol. 94, p. 219.

38. **Wang, Q. G., Apelian, D. and Lados, D. A.** *Fatigue Behavior of A356-T6 Aluminium Cast alloys. Part I: Effect of Casting Defects.* 2001, Light Metals, Vol. 1, pp. 73-84.

39. **Nyahumwa, C., Green, N. R. and Campbell, J.** *Effect of Mold-Filling Turbulence on Fatigue Properties of Cast Aluminium Alloys.* 1998, AFS Transactions, Vol. 106, pp. 215-223.

40. *http://www.foseco-steel.com.* [Online] FOSECO. http://www.foseco-steel.com.

41. *www.abb.com.* [Online] ABB. www.abb.com.

42. **Hertzberg, R. W.** *Deformation and Fracture Mechanics of Engineering Materials.* Fourth. s.l. : John Wiley & Sons, Inc., 1996. 0-471-01214-9.

43. *ASM Handbooks Online.* [Online] ASM. http://products.asminternational.org.

44. **Gottstein, G.** *Physical Foundations of Materials Science.* s.l. : Springer-Verlag Berlin Heidelberg, 2004. 3-540-40139-3.

45. Geochemical Instrumentation and Analysis . *serc.carleton.* [Online] [Cited: July 5, 2011.] http://serc.carleton.edu/.

46. photometrics. [Online] [Cited: July 5, 2011.] http://www.photometrics.net.

47. **Fang, Q. T. and Granger, D. A.** [ed.] Paul G. C. *Prediction of Pore Size Due to rejection of Hydrogen During Solidification of Aluminium Alloys.* Pennsylvania : The Minerals, Metals & Maerials Society, 1989.

48. **Atwood, A. C. and Lee, P. D.** *A three-Phase Model of Hydrogen Pore Formation during the Equiaxed Dendritic Solidification of Aluminium-Silicon Alloys.* London : s.n., 2001, Metallurgical and Materials Transactions B, Vol. 33B.

49. **Dispinar, D. and Arnberg, L.** *Porosity in Aluminium Alloy Castings.* 14th Inernational Metallurgy & Materials Congress. pp. 1088-1094.

50. **Shang, L. H.** *Prediction of Microporosity in Al-Si Castings in Low Pressure Permanent Mould Casting Using Criteria Functions.*, et al. 2004, International Journal of Cast Metals Research, Vol. 17.

51. **Campbell, J.** *Castings Practice.* s.l. : Elsevier Butterworth-Heinemann, 2004. 0750647914.

52. **Pequet, Ch., Gremaud, M. and Rappaz, M.** *Modeling of Microporosity, Macroporosity, and Pipe-Shrinkage Formation during the Solidification of Alloys Using a Mushy-Zone Refinement Method: Applications to Aluminum Alloys.* July 2002, Metallurgical and Materials Trans., Vol. 33A.

53. **Monroe, R.** *Porosity in Castings.* s.l. : Steel Founders' Society of America, 2005, AFS Trans.

54. **Thomas, P. M. and Gruzleski, J. E.** *Threshold Hydrogen for Pore Formation During the Solidification of Aluminium Alloys.* 1978, Metallurgical Trans., Vol. 9B.

55. **Samuel, A. M. and Samuel, F. H.** *Various aspects involved in the production of low-hydrogen aluminium castings.* 1992, Materials Science, Vol. 27, pp. 6533-6563.

56. **Mohanty, P. S., Samuel, F. H. and Gruzleski, J. E.** *Mechanism of Heterogeneous Nucleation of Pores in Metals and Alloys.* August 1993, Metallurgical Trans., Vol. 24A.

57. **Sabau, A. S. and Viswanathan, S.** *Microporosity Prediction in Aluminum Alloy Castings.* April 2002, Metallurgical and Materials Trans., Vol. 33B.

58. **Anson, J. P. and Gruzleski, J. E.** *The Quantitative Discrimination between Shrinkage and Gas Microporosity in Cast Aluminum Alloys Using Spatial Data Analysis.* s.l. : Elsevier Science Inc., 1999.

59. **Anson, J. P. and Gruzleski, J. E.** *The Quantitative Discrimination between Shrinkage and Gas Microporosity in Cast Aluminum Alloys Using Spatial Data Analysis.* s.l. : Elsevier Science Inc., 1999.